Stirring of Interior Potential Vorticity Gradients as a Formation Mechanism for Large Subsurface-Intensified Eddies in the Beaufort Gyre

GEORGY E. MANUCHARYAN[a] AND ANDREW L. STEWART[b]

[a] *School of Oceanography, University of Washington, Seattle, Washington*
[b] *Department of Atmospheric and Oceanic Sciences, University of California, Los Angeles, Los Angeles, California*

(Manuscript received 24 February 2021, in final form 6 August 2022)

ABSTRACT: The Beaufort Gyre (BG) is hypothesized to be partially equilibrated by those mesoscale eddies that form via baroclinic instabilities of its currents. However, our understanding of the eddy field's dependence on the mean BG currents and the role of sea ice remains incomplete. This theoretical study explores the scales and vertical structures of eddies forming specifically due to baroclinic instabilities of interior BG flows. An idealized quasigeostrophic model is used to show that flows driven only by the Ekman pumping contain no interior potential vorticity (PV) gradients and generate weak and large eddies, $\mathcal{O}(200)$ km in size, with predominantly barotropic and first baroclinic mode energy. However, flows containing realistic interior PV gradients in the Pacific halocline layer generate significantly smaller eddies of about 50 km in size, with a distinct second baroclinic mode structure and a subsurface kinetic energy maximum. The dramatic change in eddy characteristics is shown to be caused by the stirring of interior PV gradients by large-scale barotropic eddies. The sea ice–ocean drag is identified as the dominant eddy dissipation mechanism, leading to realistic subsurface maxima of eddy kinetic energy for drag coefficients higher than about 2×10^{-3}. A scaling law is developed for the eddy potential enstrophy, demonstrating that it is directly proportional to the interior PV gradient and the square root of the barotropic eddy kinetic energy. This study proposes a possible formation mechanism of large BG eddies and points to the importance of accurate representation of the interior PV gradients and eddy dissipation by ice–ocean drag in BG simulations and theory.

KEYWORDS: Arctic; Sea ice; Eddies; Potential vorticity

1. Introduction

a. Role of eddies in the Beaufort Gyre

The Beaufort Gyre (BG) is a large-scale, predominantly anticyclonic circulation in the western Arctic Ocean, the strength and shape of which vary on interannual to decadal time scales (Proshutinsky et al. 2019; Regan et al. 2019). Continuing efforts to expand the observational network in the form of in situ measurements from ships, moorings, and ice-tethered profilers, in addition to satellite observations, have shed light on many crucial BG processes (Proshutinsky et al. 2020). The gyre variability has previously been characterized as surface stress driven, with a corresponding Ekman pumping that displaces isopycnals vertically in the ocean interior and transports surface water masses toward its center (Proshutinsky et al. 2009).

Recent theoretical developments have highlighted two processes that can equilibrate the gyre against the surface stress forcing: mesoscale eddy overturning (Manucharyan et al. 2016; Manucharyan and Spall 2016) and the ice–ocean stress "governor" (Dewey et al. 2018; Zhong et al. 2018; Meneghello et al. 2018a; Doddridge et al. 2019; Wang et al. 2019). On the one hand, the equilibration by mesoscale eddies requires the Ekman-pumping-driven currents to be baroclinically unstable, generating mesoscale eddies that counteract the Ekman pumping via the eddy-induced overturning. On the other hand, when sea ice is relatively immobile, the ice–ocean stress becomes cyclonic for an anticyclonic gyre, counteracting the pumping induced by anticyclonic stresses when the ice pack is relatively loose. The actual state of the gyre is likely somewhere in between those two idealized limits, but with continuing global warming and the associated reduction of sea ice over the Beaufort Gyre, the importance of mesoscale eddies may increase (Armitage et al. 2020; Manucharyan et al. 2022).

A number of observational and modeling studies point to the necessity of eddies in explaining the observed large-scale behavior of the gyre, as was theorized by Manucharyan and Spall (2016) and Manucharyan et al. (2016). Meneghello et al. (2017) estimated the eddy tracer diffusivity from mooring velocities and found that it was sufficient to counteract the estimated surface Ekman pumping. However, Kenigson et al. (2021) pointed out that the eddy buoyancy diffusivity, rather than the eddy tracer diffusivity, is necessary to evaluate the strength of the eddy overturning, and remains to be constrained via observations. Analyzing the isopycnal motion in mooring observations, Kenigson et al. (2021) point out that neither the Ekman pumping nor vertical mixing nor boundary fluxes explain the vertical structure of the halocline, in which isopycnal slopes increase with depth through the Pacific winter layer, and conclude that eddies likely play a key role in setting the vertical structure.

Using idealized simulations, Meneghello et al. (2018a) and Doddridge et al. (2019) point out that with decreasing sea ice concentration, eddies play a larger role in gyre equilibration because of the diminishing impact of the ice–ocean governor. Meneghello et al. (2021) also highlighted the role of ice–ocean

Denotes content that is immediately available upon publication as open access.

Corresponding author: Georgy Manucharyan, gmanuch@uw.edu

DOI: 10.1175/JPO-D-21-0040.1

drag in dissipating eddy energy. Using a submesoscale-permitting global ocean model, Manucharyan and Thompson (2022) demonstrated that at concentrations beyond about 80%, sea ice plays a major role in dissipating the eddy kinetic energy in the upper ocean and affects ice–ocean heat fluxes in such a way as to cause a positive feedback. Providing the first observational estimate of the BG energy budget, Armitage et al. (2020) hypothesized that frictional eddy dissipation against the ice is required to explain the accumulation of the available potential energy after 2008, given the excess kinetic energy input from winds and ice into geostrophic currents. However, eddy characteristics inferred from in situ observations (Zhao et al. 2016) are not well correlated with the interannual BG variability, likely due to temporal or spatial sparseness of the observations. The evidence revealing the tight connection between the eddy field and the BG mean flow was recently presented by Manucharyan et al. (2022), who inferred eddy characteristics from their observed impact on the rotation rate of isolated sea ice floes in BG marginal ice zones.

Thus, a range of theoretical, observational, and modeling studies focused on different aspects of BG dynamics point to the importance of mesoscale eddies. The common argument among these studies is that the eddies need to form via baroclinic instabilities of the interior BG currents to drain their potential energy, slump the isopycnals, and counteract the Ekman-driven isopycnal steepening.

b. *Properties of BG eddies in observations and models*

Direct observations of the BG eddy field remain either spatially or temporally sparse, but eddies are nonetheless evident in in situ mooring and Ice-Tethered Profiler (ITP) hydrography (Hunkins 1974; Manley and Hunkins 1985; D'Asaro 1988; Zhao et al. 2014, 2016, 2018). Zhao et al. (2014) characterized the observed coherent eddies in the interior of the gyre by their distinct core depths, core temperature and salinity properties. The shallowest eddies in the Canada Basin are found immediately below the mixed layer, with core depths within the top 80 m and near-freezing core temperatures; it has been posited that they are generated by the instability of surface fronts (Manucharyan and Timmermans 2013). Eddies with cores between about 80 and 300 m have saltier core water and a range of core temperatures, and may be generated by the instability of boundary currents (Hunkins 1974; D'Asaro 1988; Zhao et al. 2014). Middepth eddies that were identified in moorings have double cores, one right below the Pacific halocline around 200 m and another one at the top of the Atlantic layer around 400 m. The deepest eddies are commonly found at a depth of about 1 km (Zhao and Timmermans 2015). The eddy sizes also vary, ranging from a few kilometers for submixed layer eddies up to a few tens of kilometers for deeper eddies.

In search for a better understanding of the BG eddy field, several recent studies used satellite observations, detecting eddy footprints on the surface ocean and sea ice (Kozlov et al. 2019; Cassianides et al. 2021; Manucharyan et al. 2022), as well as on sea surface height (Kubryakov et al. 2021). These satellite observations identified over 4000 open-ocean eddies and over 3500 eddies in marginal ice zones using Synthetic Aperture Radar observations (Kozlov et al. 2019) and detected over 2000 eddies using altimetric observations in ice-free regions (Kubryakov et al. 2021). Additionally, 20 000 isolated sea ice floes were detected in BG marginal ice zones, and their rotation rates were attributed to the underlying oceanic eddy field (Manucharyan et al. 2022). These numbers of eddies far exceed the few hundred eddies that were detected using in situ ITP and mooring observations (Zhao et al. 2014, 2016). Note that satellites can detect only those eddies with surface signatures; hence, most of the eddies with small localized cores in the interior of the water column are excluded from that record.

The satellite-observed eddies have a wide range of length scales, from $\mathcal{O}(5)$ km eddies detected from SAR patterns (Kozlov et al. 2019) to some eddies reaching about 120 km in diameter in altimetric observations (Kubryakov et al. 2021). Notably, the relatively large eddies that were detected from the coarse-resolution altimetry have average diameters of about 60 km and appear with no significant cyclone/anticyclone asymmetry (Kubryakov et al. 2021). A range of reconstructed eddy diameters (about 20–80 km) was estimated from sea ice floe rotation rates (Manucharyan et al. 2022). Such eddy sizes are significantly larger than the coherent vortices identified in the interior of the water column in BG moorings and ITPs (Zhao et al. 2014, 2016), but still not as large as eddies simulated in idealized BG modeling studies (Manucharyan and Spall 2016; Meneghello et al. 2018a; Spall 2020). Indeed, eddies simulated in idealized Ekman-pumping-driven BG models are commonly over 100 km in size [see, e.g., Fig. 2a in Manucharyan and Spall (2016), Fig. 2a in Meneghello et al. (2018a), and Fig. 4 in Spall (2020)]. It is plausible that eddies significantly larger than 100 km do exist but are yet to be quantified because they are generally weaker compared to the localized, small-scale eddies. However, it is also possible that the eddies generated in idealized BG models might be overly large and/or otherwise biased due to various idealizations commonly used in process studies, e.g., simplified stratification and lack of mixed layer or near-coastal dynamics.

Comprehensive mesoscale eddy-resolving global ocean or regional Arctic Ocean simulations have the advantage of representing many processes but require high spatial resolution to at least resolve the $\mathcal{O}(10)$ km Rossby deformation radius in deep basins away from continental shelves. Recently, a few studies analyzed the eddy field in comprehensive models with $\mathcal{O}(1)$ km resolution (Wang et al. 2020; Regan et al. 2020; Meneghello et al. 2021). These models reproduce qualitatively, and in many cases quantitatively, many large-scale features of the BG, including the ocean stratification, freshwater content, and mean currents. However, there are substantial discrepancies between the BG eddy simulated in these models and observations. For example, in the interior of the BG (away from continental slopes), these models predict a relatively low eddy kinetic energy in the Pacific halocline layer, $\mathcal{O}(10^{-4})$ m^2 s^{-2} at depths of 100–200 m (Wang et al. 2020; Regan et al. 2020).

In contrast, Hunkins (1974) observed EKE levels of $\mathcal{O}(6 \times 10^{-3})$ m^2 s^{-2} and similarly high EKE levels are observed

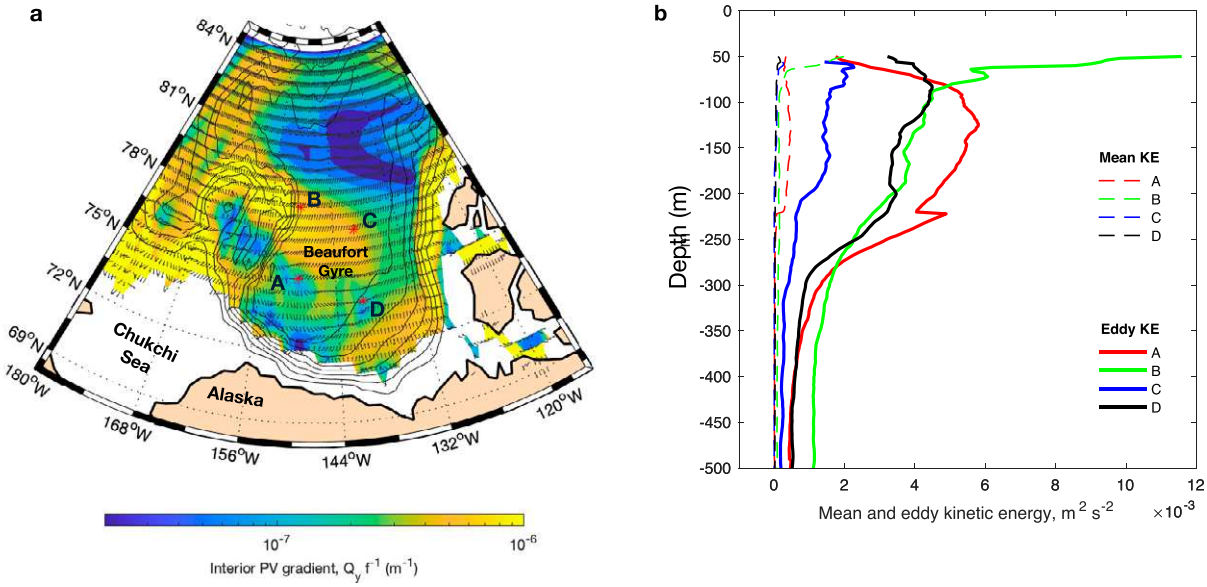

FIG. 1. Signatures of the interior PV gradients and eddy kinetic energy in the Beaufort Gyre as evident from climatological hydrographic observations and the four BGEP moorings. (a) The magnitude of the quasigeostrophic PV gradient in the Pacific winter water mass bounded by the $\sigma = 26$ and 27 kg m^{-3} isopycnals, evaluated from the July to October average of monthly climatology (MIMOC), neglecting the contribution of relative vorticity. (b) The vertical distribution of the mean and eddy kinetic energy in the four BGEP moorings. Note the overwhelming dominance of the eddy kinetic energy over the entire depth range.

in all of the Beaufort Gyre Exploration Project (BGEP) moorings (A, B, C, D), reaching (10^{-3} m^2 s^{-2}) in the deep Atlantic layer and $\mathcal{O}(5 \times 10^{-3})$ m^2 s^{-2} around 200-m depth in the Pacific layer (Fig. 1). The EKE in those comprehensive models is so low as to become of the same order of magnitude as the mean kinetic energy (Regan et al. 2020). However, as we show here, this is in stark contrast with BGEP mooring observations where the EKE is at least an order of magnitude larger than the mean KE (Fig. 1b). Furthermore, the 1 km simulation analyzed in Wang et al. (2020) generated a vertical EKE profile that has two narrow peaks: one below the mixed layer and another within the Pacific halocline. This also stands in sharp contrast with the mooring observations, in which the EKE is concentrated approximately between 50 and 250 m deep (with the exception of mooring B, which additionally shows a strong surface EKE peak). Thus, there are significant discrepancies between the observed and simulated eddy fields, which are difficult to explain due to our gaps in understanding of how the BG eddy field relates to the large-scale currents and stratification. This motivates further theoretical investigations of eddy dynamics to guide quantitative analyses of eddy characteristics and formation mechanisms in both observations and eddy-resolving ocean models.

c. *Formation mechanisms of BG eddies*

Previous studies have suggested various formation mechanisms to explain the presence of eddies in the BG, including hydrodynamic instabilities associated with localized boundary currents (Hunkins 1974; Spall et al. 2008), outcropping fronts (Manucharyan and Timmermans 2013), and convection due to surface buoyancy fluxes under leads (Smith et al. 2002). The uniqueness of the BG eddies found in ITP and mooring records is that they are predominantly anticyclones with relatively cold cores. For submixed layer eddies, this can be explained if they are formed via subduction processes at outcropping fronts (Manucharyan and Timmermans 2013). The middepth anticyclonic eddies can be explained if they are forming at coastal boundary currents where low potential vorticity water masses are sustained by winds, frictional effects, and mixing (D'Asaro 1988; Spall et al. 2008), provided that eddies propagate from their coastal sites toward the interior of the gyre where they are commonly observed. The energy input associated with eddy generation is balanced by eddy dissipation processes that could be due to lateral and vertical mixing in the interior, and/or due to frictional spindown due to sea ice–ocean drag in the surface boundary layer. The eddy dissipation by the sea ice is evident in in situ observations (Hunkins 1974) and modeling studies (Brannigan et al. 2017; Wang et al. 2020; Regan et al. 2020; Meneghello et al. 2021; Manucharyan and Thompson 2022).

However, many proposed eddy formation mechanisms do not involve baroclinic instabilities in the BG interior, making it difficult to determine the role of such eddies in the gyre equilibration. Specifically, the eddy equilibration hypothesis requires that the Eulerian (Ekman-pumping-driven) overturning streamfunction be counteracted by an eddy-driven overturning streamfunction in the interior of the gyre (Manucharyan and Spall 2016; Manucharyan et al. 2017). But the eddy streamfunction is proportional to the eddy-driven isopycnal layer thickness fluxes, and the presence of those fluxes is an inherent signature of baroclinic instabilities that drain the potential energy of the flow. The nonacceleration result for geostrophic turbulence

(see Vallis 2017) implies that, in the absence of instabilities supporting the growth of eddies, weakly decaying turbulence does not affect the mean flow and does not significantly contribute to the eddy thickness fluxes. Thus, those eddies that were not formed due to baroclinic instability of the interior flows (e.g., those that have formed at the boundary currents and propagated into the interior of the gyre or formed at outcropping mixed layer fronts) are not expected to contribute to the eddy overturning in the interior of the gyre. Furthermore, baroclinic instability of the interior BG halocline (that does not outcrop) describes exponential growth of wave-like disturbances and thus is not expected to generate a substantially asymmetric cyclone–anticyclone distribution.

Therefore, the ubiquitous observations of predominantly cold-core anticyclonic BG eddies that are relatively isolated from one another imply that those eddies have likely formed elsewhere and propagated into the BG interior as a form of weakly decaying turbulence, which is known to lead to more isolated and symmetric eddies compared to those in regions of active eddy generation and interaction (McCalpin 1987; McWilliams 1990; Pavía and López 1994). This leads to a seeming contradiction: the eddy equilibration hypothesis requires eddies to be formed in the interior of the BG halocline, while the properties of the observed halocline eddies indicate that they likely have remote origins. A hypothesis reconciling this contradiction could be that the eddies associated with the baroclinic instabilities in the BG interior are relatively large and weak, such that they could appear as a background variability on top of which the strong and localized eddies stand out. Understanding the baroclinic instability of BG currents is necessary to test this hypothesis.

Several studies explored the possibility of BG eddy formation via linear baroclinic instability theory. Applying an Eady model of baroclinic instability (Eady 1949) to interior BG currents with vertical shear of about 1 cm s^{-1} (100 m)$^{-1}$, Hunkins (1974) estimated the baroclinic eddy growth rate to be approximately one month. Hunkins (1974) argued that this time scale is too long to explain the frequent eddy observations, even though the eddies appear to be of the same length scale as the deformation radius. Hart and Killworth (1976) conducted a theoretical baroclinic instability analysis, taking the stratification and velocity profiles as exponentially decaying with depth. They concluded that the baroclinic instability of the interior BG currents (idealized to have exponential profiles) requires length scales to be 10–20 times larger than the Rossby deformation radius. Both Hart and Killworth (1976) and Hunkins (1974) concluded that eddies must be forming elsewhere, in shallower regions with much larger shear. Analyzing comprehensive eddy observations, Manley and Hunkins (1985) demonstrated that eddies have temperature/salinity signatures distinct from their environment and concluded that the observed eddies likely form at the Alaskan Coastal Current and are then advected into the interior of the BG by large-scale currents. Instabilities of the coastal currents were later simulated by Spall et al. (2008) and were shown to be adequate in explaining the key properties of the observed BG anticyclones.

Recently, the baroclinic instability problem of interior BG currents was revisited in Meneghello et al. (2021), who used a more realistic representation of BG stratification but kept an idealized exponential velocity profile. Three instability modes were found: the surface mode localized in the mixed layer and strongly affected by sea ice dissipation, the deep mode in the abyssal ocean, and the halocline mode localized in the Pacific halocline layer. The halocline mode had a vertical structure similar to the eddy profiles observed in moorings, which led the authors to speculate that this instability mode could explain the origin of the eddies observed in moorings. However, the growth rate for the halocline instability mode was found to be about 2 months, similar to the estimates in Hunkins (1974) and Hart and Killworth (1976), who, in contrast, concluded that a growth time scale on the order of a month is too long to explain the observed eddies. We note that these studies explored idealized velocity and/or stratification profiles, but it might be necessary to use more realistic profiles to correctly interpret the observed eddy field. Also, the limitation of the linear baroclinic instability theory is that it does not provide any information about the strength of equilibrated eddies and commonly underestimates their length scales (Smith 2007) because it does not take into account the nonlinear eddy interactions that lead to the inverse energy cascade toward larger length scales and lower baroclinic modes (Smith and Vallis 2001; Zhao et al. 2018). Thus, the eddy formation via local baroclinic instability in the BG interior still requires better understanding.

d. *Purpose of this study*

This study explores the characteristics of eddies that could form due to baroclinic instabilities of the interior BG currents, as only those eddies are expected to be explicitly counteracting the Ekman pumping. We attempt to reconcile the discrepancy in length scales between the idealized model eddies and satellite observations by proposing an eddy-formation mechanism that leads to the coexistence of eddies with distinct length scales. Specifically, we will demonstrate below that the Pacific halocline layer in the BG contains interior potential vorticity (PV) gradients (Fig. 1a) and those gradients can dramatically reduce the length scales and enhance the energy of eddies generated from local baroclinic instabilities.

The manuscript is organized as follows: section 2 discusses the vertical profile of the flows pertinent to the BG, pointing out the associated interior PV gradients and the inability of the Ekman pumping to generate them. In section 3 we use quasigeostrophic linear stability analysis to investigate whether linear growth of baroclinic waves can account for the observed structure of BG eddies. In section 4 we present numerical simulations of an idealized three-layer quasigeostrophic model with a range of background flow profiles. In section 5 we show that in these simulations, interior PV gradient and ice–ocean drag play crucial roles in generating small-scale subsurface-intensified eddies. In section 6 we propose the eddy formation mechanism, supporting it with the scaling law based on the analysis of the potential enstrophy budget, directly connecting the existence of the smaller-scale subsurface-intensified eddies to the background PV gradient and the strength of the larger-scale barotropic eddies. Finally, in section 7 we summarize the

results, outline the key limitations of the study, and discuss our proposed paradigm of the BG eddy field with implications for the BG eddy equilibration hypothesis.

2. Baroclinic shear of the Ekman-driven gyre

Previous theories of the BG circulation have typically characterized it as being forced by surface stresses, leading to Ekman pumping that displaces isopycnals in the interior of the water column (e.g., Proshutinsky et al. 2009; Meneghello et al. 2018a; Doddridge et al. 2019; Manucharyan et al. 2016, 2017; Manucharyan and Spall 2016; Manucharyan and Isachsen 2019). The surface-stress-driven Ekman pumping has counteracting components due to the ice–ocean stress and atmosphere-ocean stress (Meneghello et al. 2018b; Doddridge et al. 2019). Considering that length scale of the surface Ekman pumping is significantly larger than the deformation radius, and due to a relatively weak beta effect at such high latitudes, the Ekman-pumping-driven Eulerian-mean vertical velocity does not dramatically decrease with depth (as it occurs in midlatitude gyres) and can penetrate all the way to the bottom boundary layer of the water column (Manucharyan and Isachsen 2019; Kenigson et al. 2021). Importantly, the strong vertical velocity is present across the BG halocline, which is evident in idealized numerical simulations [Figs. 5 and 6 of Manucharyan and Isachsen (2019)], comprehensive ocean models [Fig. 1 in Liang et al. (2017)], and analytical solutions for the BG stratification [Fig. 6b in Kenigson et al. (2021)].

If isopycnal displacements at depth were solely due to the nearly depth-independent Ekman-pumping-induced vertical velocity, the isopycnals would remain roughly parallel to each other, leading to a state with zero interior PV gradients (Kenigson et al. 2021). Indeed, since the stress occurs at the surface, it can only explicitly affect the PV gradients in the surface mixed layer, leaving the interior PV intact. This key observation allows one to estimate the expected vertical structure of the mean flow from the density stratification.

Consider a situation in which the slopes of the gyre's isopycnals have been generated by vertically displacing the isopycnals that were initially horizontal. The local buoyancy anomaly $b(z, \mathbf{x})$ can then be expressed as

$$b = \overline{b}_z(z)h(\mathbf{x}). \tag{1}$$

Here $\overline{b}_z = N^2(z)$ is the mean stratification and $h(\mathbf{x})$ is the vertical isopycnal displacement, which is the same for all depths and only depends on the horizontal location $\mathbf{x}$, following that $h_t = w_{\text{Ekman}}(\mathbf{x})$. Using the thermal wind balance we obtain that $f\mathbf{k} \times \mathbf{u}_z = -\nabla b$, where ∇ denotes the horizontal gradient vector and f is the Coriolis parameter. Taking the isopycnal depth gradient to be directed along the x axis, the baroclinic shear of the y-direction velocity v is $v_z = b_x f^{-1} = \overline{b}_z(z)h_x f^{-1}$ and the velocity itself is determined after vertical integration as

$$v(z) = v_0 + \overline{b}(z)f^{-1}h_x. \tag{2}$$

Here $h_x(x)$ does not depend on the depth, and v_0 is the deep ocean flow where $\overline{b}_z \approx 0$. Thus, the vertical structure of the mean flow for a gyre driven solely by surface stresses should be simply proportional to its buoyancy anomaly, i.e., $v(z) \sim \overline{b}(z)$. Note that such a profile implies zero isopycnal PV gradients: neglecting the planetary vorticity gradient, the quasigeostrophic PV may be written as

$$\frac{\partial q}{\partial x} \approx \frac{\partial}{\partial z}\left(\frac{f^2}{\overline{b}_z}\frac{\partial v}{\partial z}\right). \tag{3}$$

Substituting (2) into (3) yields $\partial q/\partial x = 0$. Note that the layer-averaged quasigeostrophic PV gradient is simply proportional to the difference between the isopycnal slopes bounding the layer. Thus, the presence of the interior PV gradients can be inferred either from the deviations of the mean flow profile from (2) or, equivalently, from the presence of nonparallel isopycnals bounding the Pacific halocline layer.

We now explore the observed vertical structure of the BG mean flow and point out its similarities and deviations from the zero PV gradient solution. The velocity measurements come from long-term ADCP and CTD data at the four BG moorings (A, B, C, D) that are sustained as part of the Beaufort Gyre Exploration Program (Proshutinsky et al. 2009). The moorings are located in the interior of the BG (Fig. 1a) where the mean flow is not as strong as at the edges of the gyre, but these measurements nonetheless provide critical information about the vertical structure of the currents.

We present the mean velocity observations by aligning the x axis of our coordinate in the direction of the strongest surface flow. Since mooring observations do not provide the information about the large-scale horizontal gradient in isopycnal depth, it is instructive to view the mooring observations using $[u(z), b(z)]$ diagrams (Fig. 2). In all four moorings, there is a clear distinction between the deep Atlantic water mass (below about 350 m) and the Pacific water mass above it, seen not only in the potential density profile but also in the velocity profile (Fig. 2a). Both Atlantic and Pacific water masses, with approximate potential densities ranges of about (24.5, 27.5) kg m^{-3} and (27.5, 28) kg m^{-3}, generally follow the linear relation between the mean velocity and the buoyancy in moorings C and D, while moorings A and B exhibit substantial deviations, particularly in the Pacific halocline and near-surface layers (Fig. 2b). Specifically, relative to the potential density profile, the velocity profile in mooring A exhibits an overly strong subsurface flow in the depth range of 100–200 m. In contrast, mooring B exhibits a relatively weak flow.

These deviations imply that processes other than Ekman pumping are actively present in the Pacific and near-surface layers. The surface layer, extending to about 60–80 m, is expected to deviate from the Ekman solution due to surface buoyancy forcing, enhanced vertical diffusivity, and eddy viscosity in the mixed layer due to ice–ocean drag—all of which act as PV sources for isopycnal layers that even temporarily outcrop to the surface. In the Pacific layer, the PV gradients could emerge from a lateral injection of water masses or due to eddies with vertically varying eddy diffusivity (Kenigson et al. 2021). Critically, any deviations of the velocity profile from the potential density profile signify

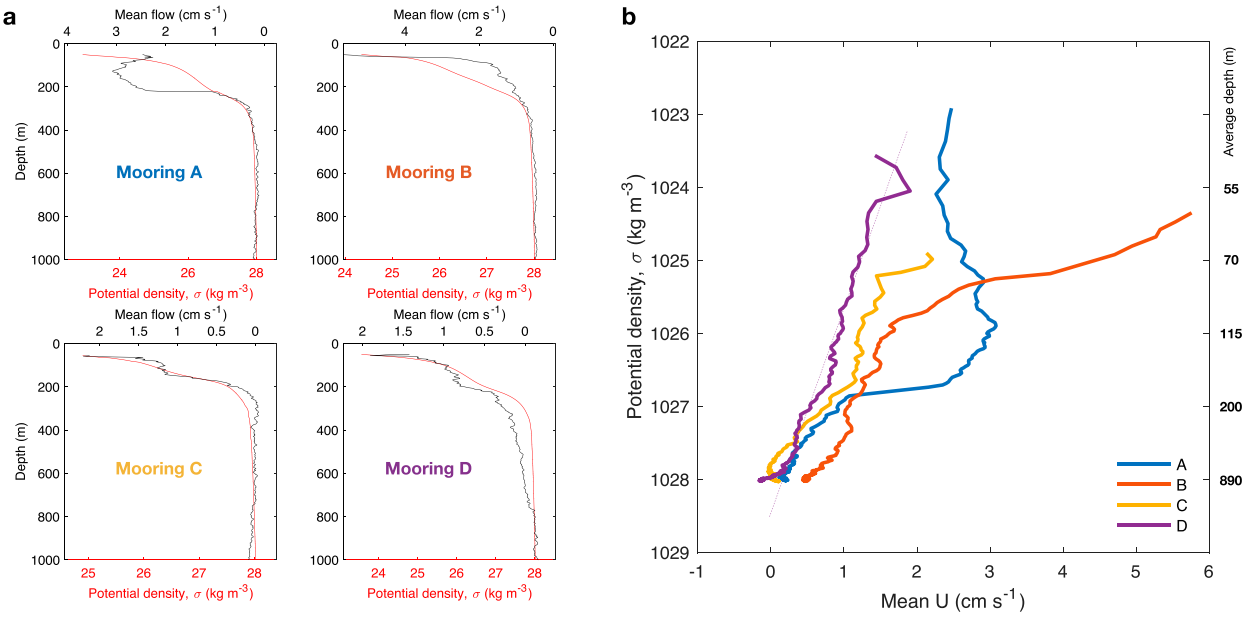

FIG. 2. Characteristics of the vertical profiles of mean ocean currents and potential densities estimated for the four BGEP moorings A, B, C, and D, with their locations denoted with red stars in Fig. 1a. (a) Panels show the mean horizontal flow (black, top x axis) and the potential density (red, bottom x axis) as measured by the BGEP moorings. (b) The time-averaged profiles of horizontal currents and potential density are plotted against each other. The component of the mean flow in the direction of the strongest upper ocean currents is plotted, and the weaker mean flow component in the orthogonal direction has been omitted. The right y axis shows the depths corresponding to the mean potential density profile over all moorings. A linear fit is shown for reference for mooring D. Note that deviation from linear dependency between the density and mean flow is a signature of interior PV gradients [see Eq. (2)].

the presence of the interior PV gradients that can affect the flow stability.

The PV gradients can be estimated from either the climatological distribution of isopycnal layer thicknesses or the long-term mean velocity profiles in moorings. We calculate the quasigeostrophic PV gradients for the Pacific halocline layer derived from a climatological hydrography, the Monthly Isopycnal and Mixed-Layer Ocean Climatology (MIMOC) dataset (Johnson et al. 2012), as $\nabla Q/f_0 = -\nabla h/\langle h\rangle$, where h is the thickness of the isopycnal layer bounded by potential densities $\sigma_1 = 26$ kg m^{-3} and $\sigma_2 = 27$ kg m^{-3}, and $\langle h\rangle$ is its average over the gyre (Fig. 1a). The PV gradients for the Pacific layer are strong near prominent bathymetric features, e.g., continental slopes, Northwind Ridge, and Chukchi Plateau, where Q_{2y}/f ranges from 1×10^{-6} to 4×10^{-6} m^{-1}. The BG interior also has elevated PV gradients, with $Q_{2y}/f = 0.4 \times 10^{-6}$ m^{-1} on average within the gyre. The weakest PV gradients are found in regions of cyclonic circulation at the northern edge of the gyre (centered at about 81°N), with $Q_{2y}/f < 1 \times 10^{-7}$ m^{-1}. Interior PV gradients can also be estimated from mooring velocity and stratification data using Eq. (3); averaged in the halocline layer between 80 and 250 m, Q_{2y}/f is about 1×10^{-6} m^{-1} for moorings A and B, but it is $<1 \times 10^{-7}$ m^{-1} in moorings C and D, which is significantly lower than its estimate using the climatology. The discrepancy could be due to mooring observations reflecting only a point measurement that might not be representative of a large area, as is the case with the highly smoothed climatology.

We also note that calculating the PV from mooring velocities using its continuously stratified quasigeostrophic definition leads to noisy profiles even after smoothing the stratification and velocity profiles with low-order splines. Consequently, the stability analysis might lead to unstable modes that are not necessarily present in the real ocean and are simply an artifact of specifying a noisy background PV gradient profile. This motivates us to explore the BG dynamics as a simple three-layer system that explicitly prohibits any vertical structure within each layer and allows focusing on eddies that are large enough to affect the entire Pacific halocline layer. But, since the mean BG currents are heterogeneous, we will conduct a sensitivity study exploring the eddy field forming due to a range of idealized velocity profiles.

3. Linear instabilities of Beaufort Gyre–like flows

The baroclinic instability of profiles with zero interior PV gradients is a version of the so-called Eady problem (Eady 1949), in which the instability emerges due to resonant interactions of the edge waves generated at the very surface and bottom of the ocean (Vallis 2017). The presence of interior PV gradients allows the formation of an interior Rossby wave that can interact with the surface edge wave to generate the instability—this is a version of the so-called Charney problem, in which the interior PV gradient is due to the beta effect (Charney 1947). Since mean flows with no interior PV gradients profiles present a special case from the perspectives of

the Ekman-driven BG dynamics and the baroclinic instability, we will use those profiles as a baseline for comparison of eddy characteristics between different profiles.

In section 2 we showed that the BG mean flow and potential density profiles generally deviate from the linear relation, implying that the gyre maintains interior PV gradients. This has also been pointed out by Kenigson et al. (2021) and Meneghello et al. (2021). The mean BG isopycnals are not parallel, and their slopes increase in magnitude down to about 200-m depth. This increase is also evident in the transient gyre evolution, in which the isopycnal depths are correlated with the Pacific halocline layer thickness (Kenigson et al. 2021). This implies that the interior PV gradients are time dependent and likely coupled with the gyre and eddy dynamics. In this paper, however, we simplify the problem by investigating the implications of these interior PV gradients for eddy characteristics in an uncoupled way.

We represent the key features of the stratification and velocity profiles using an idealized three-layer quasigeostrophic (QG) flow corresponding approximately to the surface (0–80 m), Pacific (80–250 m), and abyssal (250–4000 m) layers. The advantage of the three-layer idealization is that it offers a minimum level of complexity required to represent the interior PV gradients. It is also motivated by several dynamical considerations: the BG potential density has strong gradients at the base of the mixed layer, in the Pacific halocline layer, and much weaker gradients in the Atlantic and abyssal layers. Since we are interested in explaining the properties of eddies that could contribute to the gyre equilibration, those eddies must be forming and occupying the entire Pacific layer, which we must therefore include in our idealized model. The surface mixed layer is essential to allow ice–ocean drag to dissipate eddy kinetic energy—a crucial process necessary for eddy equilibration. And the bottom layer represents the abyssal ocean, essential for the development of instabilities in flows with zero interior PV gradients; for such flows, the very top and bottom layers are the only layers capable of carrying PV anomalies. The three-layer truncation is motivated by moored measurements of the kinetic energy in the Beaufort Gyre that has a relatively simple vertical profile, being concentrated in the Pacific halocline layer (depths between about 50 and 250 m) and substantially weaker in the surface mixed layer and the abyssal ocean (Fig. 1b). In addition, as was shown in Zhao et al. (2018), the EKE in BG moorings is dominated by the barotropic and first two baroclinic modes. Thus, the three-layer QG model is aimed at representing large-scale eddies occupying the entire Pacific halocline layer (the focus of our study), with the limitation that it cannot represent the development of eddies with vertical scales smaller than the selected layer thicknesses, for example localized eddy cores inside the layers (Zhao et al. 2014; Zhao and Timmermans 2015).

a. *Quasigeostrophic model formulation*

We represent the vertical structure of the BG with three isopycnal layers: a surface layer of thickness $H_1 = 80$ m and $\rho_1 = 1025$ kg m^{-3}, a middle halocline layer with $H_2 = 170$ m and $\rho_2 = 1027.5$ kg m^{-3}, and a deep layer with $H_3 = 3750$ m and $\rho_3 = 1028$ kg m^{-3}. The stratification parameters for the three-layer quasigeostrophic model are estimated from the observed profiles of the potential density (see Fig. 2). The first and second baroclinic Rossby deformation radii are $R_{d1} = 12.7$ km and $R_{d2} = 6.3$ km, which are approximately consistent with observational estimates (Nurser and Bacon 2014; Zhao et al. 2014).

The flow in each of the three isopycnal layers is assumed to obey quasigeostrophic dynamics (e.g., Vallis 2017). We introduce the QG potential vorticity in each layer, q_i, where i is the layer index counting from the top. The PV in each layer is related to a corresponding streamfunction ψ_i as follows:

$$q_1 = \beta y + \nabla^2\psi_1 + \frac{f_0^2}{H_1}\left(\frac{\psi_2 - \psi_1}{g_1'}\right), \tag{4a}$$

$$q_2 = \beta y + \nabla^2\psi_2 + \frac{f_0^2}{H_2}\left(\frac{\psi_1 - \psi_2}{g_1'} - \frac{\psi_2 - \psi_3}{g_2'}\right), \tag{4b}$$

$$q_3 = \beta y + \nabla^2\psi_3 + \frac{f_0^2}{H_3}\left(\frac{\psi_2 - \psi_3}{g_2'}\right). \tag{4c}$$

Here f_0 and β are the Coriolis and beta plane parameters, with reference values of 1.4×10^{-4} s^{-1} and 10^{-13} m^{-1} s^{-1}, respectively. We denote the reference thicknesses of each layer as H_i, and the reduced gravity at each layer interface as $g_1' = g_0(\rho_2 - \rho_1)/\rho_3$ and $g_2' = g_0(\rho_3 - \rho_2)/\rho_3$, where $g_0 = 9.81$ m s^{-2} is the gravitational acceleration.

In our linear stability calculations, as well as in our nonlinear numerical simulations in sections 4 and 5, (4a)–(4c) describe perturbations relative to zonal background flow in each layer (U_i) that is stationary and horizontally homogeneous such that

$$\overline{\psi}_i = -U_i y. \tag{5}$$

The corresponding background PV gradients Q_{iy} are computed from (4a)–(4c), taking into account that for the spatially uniform background flow we have $\nabla^2\overline{\psi}_i = 0$. For example, the background PV gradient in the second layer is defined as

$$Q_{2y} = \beta + \frac{f_0^2}{H_2}\left(\frac{-U_1 + U_2}{g_1'} - \frac{-U_2 + U_3}{g_2'}\right), \tag{6}$$

which can be estimated from mooring observations using layer-averaged velocities U_i in the direction of the gyre, assuming that long-term average velocities are approximately geostrophic. Note that we neglect the effect of bottom topographic slopes, which would modify the PV gradient in the lowest layer. The perturbation PV in each isopycnal layer evolves according to

$$\frac{Dq_i}{Dt} = \frac{\partial q_i}{\partial t} + (\mathbf{u}_i + \mathbf{U}_i)\cdot\nabla q_i + v_i Q_{iy} = S_i, \tag{7}$$

where the mean flow vector $\mathbf{U}_i$ is aligned in the x direction and has amplitude U_i.

The terms S_i in (7) denote nonconservative effects. In our linear stability calculations, we parameterize the effects of

friction against the sea ice via a linear drag, and we neglect frictional damping at the sea floor:

$$S_1 = -r_1 \nabla^2 \psi_1, \tag{8a}$$

$$S_2 = 0, \tag{8b}$$

$$S_3 = 0. \tag{8c}$$

We use a reference value of $r_1 = 0.2$ days^{-1}, corresponding to a surface Ekman layer thickness of approximately 4 m (Vallis 2017; Meneghello et al. 2020). Note that this is a highly simplified representation of ice–ocean stresses (e.g., McPhee 2012; Cole et al. 2014), which we use to allow linearization of the equations of motion; in section 5 we conduct numerical simulations using a more realistic, quadratic formulation of the frictional stresses. We found that including a linear bottom drag yielded a negligible change in the unstable modes. However, the ice–ocean drag is expected to play a crucial role in determining equilibrium eddy characteristics in nonlinear simulations (Manucharyan and Thompson 2022).

We define a set of background velocity profiles in the three isopycnal layers as $(U_1, U_2, 0)$, making the simplifying assumption that the deep ocean velocity is zero (see Fig. 2). In the more general case of nonzero bottom flow, one could switch to a reference frame that translates zonally at the speed of the bottom flow, resulting in a velocity profile $(U_1 - U_3, U_2 - U_3, 0)$ in the moving frame. Thus, only two mean flow parameters determine the modes of baroclinic instability: the surface mean flow U_1, and the upper-ocean shear $\Delta U = U_1 - U_2$. Based on the mooring observations shown in Fig. 2, we select an upper-layer mean flow of $U_1 = 3$ cm s^{-1}. We use a range of ΔU to explore velocity profiles ranging from strongly surface-intensified flows (e.g., mooring B) to flows with a pronounced subsurface velocity maximum (e.g., mooring A). For reference, the purely Ekman-driven solution with zero PV gradient in the second layer corresponds to $\Delta U = U_1/(1 + g_2/g_1) = 2.5$ cm s^{-1}. Profiles with near-vanishing interior PV gradients correspond to a linear relation between the potential density and velocity profiles, as approximately occurs at moorings C and D (see Fig. 1).

b. Linear stability formulation

We formulate the linear stability problem by linearizing the PV conservation equations, considering periodic solutions with a range of wavenumbers, and solving the resulting eigenvalue problem to obtain the corresponding growth rates. The linearized PV conservation equation is

$$\frac{\partial \mathbf{q}}{\partial t} = -\mathbf{U} \cdot \frac{\partial \mathbf{q}}{\partial x} - \frac{\partial \psi}{\partial x} \cdot \mathbf{Q}_y - \mathbf{r} \cdot \nabla^2 \psi. \tag{9}$$

Here we have switched our notation to simplify the presentation of the following equations: vectors now describe the vertical structure of the corresponding quantity, e.g., $\mathbf{q} = \{q_i, i = 1, \ldots, 3\}$, From (4a)–(4c), the PV depends on the streamfunction via $\mathbf{q} = \nabla^2 \psi + \mathbf{L} \cdot \psi$, where $\mathbf{L}$ is a matrix containing the coefficients of the stretching component of the PV. The streamfunction can therefore be expressed in terms of the PV as $\psi = (\nabla^2 + \mathbf{L})^{-1} \cdot \mathbf{q}$.

We seek solutions of the form $\mathbf{q} = \Re[\tilde{\mathbf{q}} \exp(ikx) \exp(\lambda t)]$, which describes a zonal baroclinic wave with wavenumber k and growth rate λ. This simplifies the relationship between the PV and streamfunction to $\tilde{\boldsymbol{\psi}} = (-k^2\mathbf{I} + \mathbf{L})^{-1} \cdot \tilde{\mathbf{q}}$, where $\mathbf{I}$ denotes the identity matrix. The linearized PV evolution Eq. (9) can then be written as

$$[-ik\mathrm{diag}(\mathbf{U}) - ik\mathrm{diag}(\mathbf{Q}_y)(-k^2\mathbf{I} + \mathbf{L})^{-1} + k^2 \mathrm{diag}(\mathbf{r}) \cdot (-k^2\mathbf{I} + \mathbf{L})^{-1}] \cdot \tilde{\mathbf{q}} = \lambda \tilde{\mathbf{q}}, \tag{10}$$

where "diag" denotes the construction of a diagonal matrix from a vector. Thus, the problem of identifying the growth rates λ and the corresponding vertical structures $\tilde{\mathbf{q}}$ reduces to identifying eigenvalues and corresponding eigenfunctions of the matrix operator given by the left-hand side of (10).

c. Stability characteristics

In Figs. 3a and 3b we map the growth rate λ as a function of the zonal wavenumber k, and also as a function of the upper-ocean shear ΔU. This reveals multiple instability "branches," depending on the sign and magnitude of ΔU. The gravest unstable mode, with wavenumber $kR_{d1} < 1$, persists throughout the entire range of velocity shears ΔU. The vertical structure of this unstable mode (not shown) is similar to that of the first baroclinic mode (see section 6), i.e., having a single zero crossing in the horizontal velocity field within the halocline. A key feature of this instability branch is that at velocity shears corresponding to purely Ekman-driven currents (i.e., having zero PV gradient in the middle layer), the growth rates are minimized, with an exponential growth time scale of several months (Fig. 3c). The growth rates increase quasi-linearly with the magnitude of the middle-layer PV gradient, reaching exponential growth time scales of ~10 days for the largest upper-ocean shears considered here. We define the eddy scale corresponding to the most unstable mode as π/k_m, where k_m is the corresponding wavenumber. The eddy scale is maximized in the Ekman-driven case (the Eady problem), reaching ~120 km (Figs. 3d), and decreasing to ~40 km for the strongest shears considered here. Note that the resulting eddies are expected to be even larger due to the inverse energy cascade (see section 5).

For nonzero interior PV gradients, i.e., for deviations from a purely Ekman-driven flow, two additional instability branches emerge at higher wavenumbers (Figs. 3a,b). One branch occurs when there is subsurface velocity maximum, $U_2 > U_1$ [region below the red dashed line in Figs. 3a and 3b; the other branch occurs when the PV gradient in deepest layer flips sign, i.e., $U_2 < U_3$ (region above the blue dashed line in Figs. 3a,b). The growth rates associated with these higher-wavenumber branches are smaller than those of the low-wavenumber branch (Fig. 3c), but the associated eddy sizes are much smaller, around 10–30 km (Fig. 3d).

In Fig. 3 we additionally contrast the linear growth rates with and without linear surface friction, parameterizing the effect of drag against sea ice, and with and without the inclusion of the planetary PV gradient β. Figures 3a and 3b show that

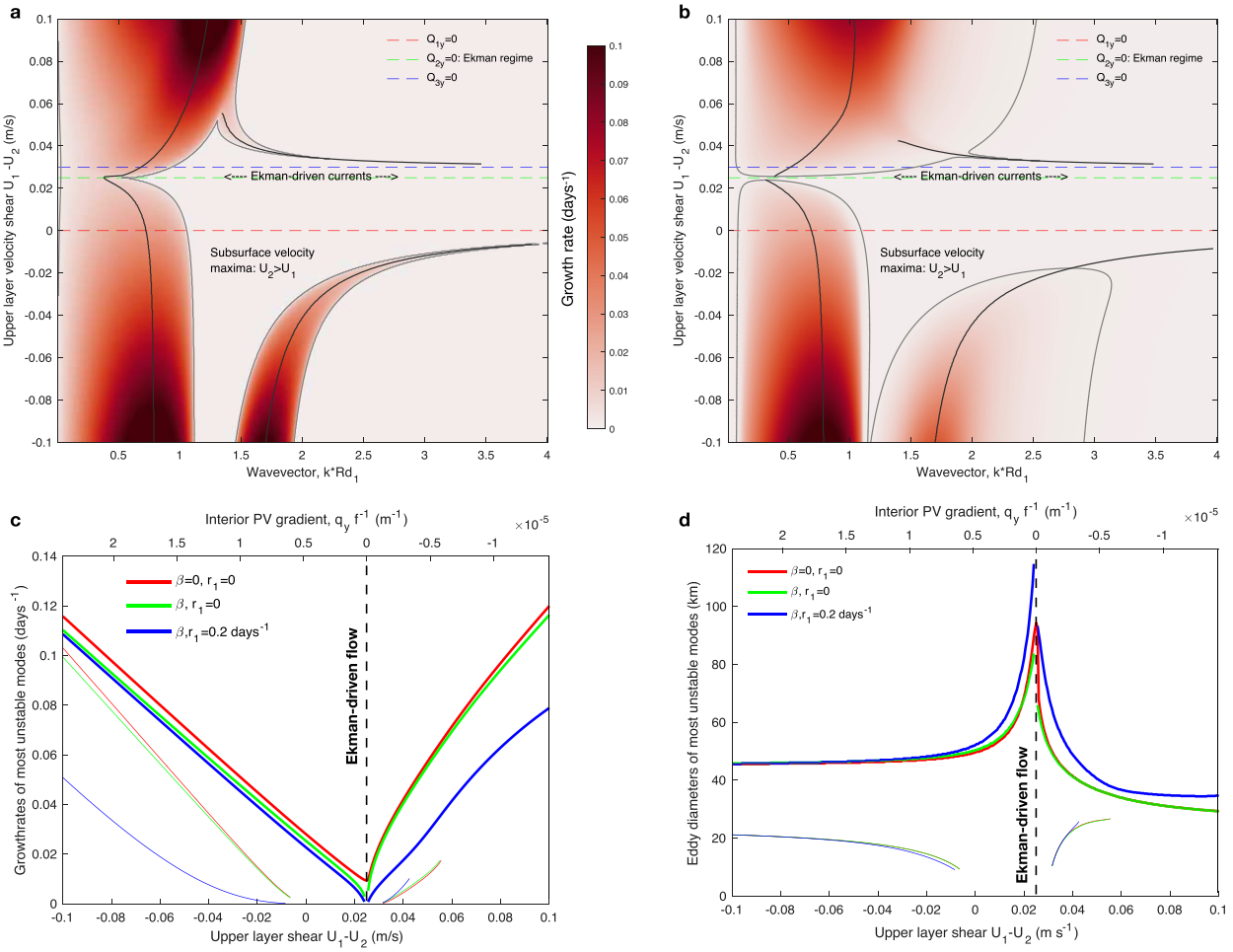

FIG. 3. Growth rates of unstable quasigeostrophic waves in a three-layer ocean. We fix the mean flow in the top layer at 0.03 m s^{-1} and impose zero mean flow in the bottom layer, then vary the middle layer velocity (quantified by the shear $\Delta U = U_1 - U_2$). (a),(b) Growth rates on an f plane at 75°N as a function of horizontal wavenumber (k) and ΔU, with the linear surface drag coefficient set to $r_1 = 0$ in (a) and $r_1 = 0.2$ days^{-1} in (b). (c) Maximum growth rates and (d) corresponding eddy diameter in each instability branch (see section 3), as functions of ΔU. The eddy diameter is calculated as $\pi/k_{\max}$ where $k_{\max}$ is the wavenumber corresponding to the maximum growth rate. Colored curves correspond to an f plane with no surface drag (red), a β plane with no surface drag (green), and a β plane with a surface drag of $r_1 = 0.2$ days^{-1} (blue). Thick and thin lines correspond to the growth rates of the low- and high-wavenumber unstable modes, respectively. All cases correspond to a latitude of 75°N.

the inclusion of surface friction does not qualitatively change the dependence of the low-wavenumber and high-wavenumber unstable modes on the upper-ocean shear ΔU. An exception is the case of zero interior PV gradient, a purely Ekman-driven flow, in which case the flow is linearly stable. For nonzero interior PV gradients, the growth rates are generally reduced, particularly in the low-wavenumber mode for positive ΔU and in the high-wavenumber mode for low ΔU (Fig. 3c). The wavelength of the low-wavenumber unstable mode increases by up to ~25% when surface friction is included (Fig. 3d). Figures 3c and 3d also show that including the planetary PV gradient has almost no discernible impact on the growth rates and length scales of the low- and high-wavenumber unstable modes.

These findings are qualitatively consistent with those of Meneghello et al. (2021), who performed linear stability analysis using a continuous vertical profile of horizontal PV gradient from the Beaufort Gyre. They found that introducing an ocean–sea ice Ekman layer only served to damp an unstable "surface mode" confined to the top ~10 m of the water column, leaving other unstable modes largely unaffected. However, despite having minimal effects on the linear stability characteristics, the ice–ocean stress will play a crucial role in suppressing the equilibrium eddy kinetic energy by providing a major source of energy dissipation to balance the energy input from baroclinic instability (see section 5).

In summary, our linear stability analysis indicates that Beaufort Gyre–like flows should be dominated by low-wavenumber (eddy scale ~50–100 km) instabilities, regardless of whether the flow is damped by friction against the overlying sea ice, and that these instabilities should grow more rapidly

at smaller scales as the interior PV gradient increases. For sufficiently large interior PV gradients, additional, slower-growing modes emerge at smaller scales (~10–30 km). However, the smaller-scale instability branches only exist for extreme interior PV gradients, larger than any of those shown in Fig. 1a. Only the PV gradient inferred from mooring A with subsurface velocity maximum ($\Delta U < 0$) may be large enough to activate the small-scale instabilities shown in Fig. 3. This suggests that the presence of small, subsurface-intensified eddies in the BG is likely not explained by the local linear growth of unstable waves and motivates exploration of the nonlinear dynamics.

4. Numerical experiments

In section 3 we showed that the growth of relatively small, subsurface-intensified eddies is consistently slower than those of larger-scale, surface-intensified eddies. This is true even in the presence of a sea ice–ocean drag that retards near-surface flows, as the subsurface-intensified wave modes are linearly stable for sufficiently small interior PV gradients. However, the linear stability theory does not necessarily explain the characteristics of the equilibrated eddy field (Smith 2007). Hence, we perform a series of numerical simulations of the fully nonlinear three-layer quasigeostrophic equations.

We configure our simulations to match the posing of our linear stability analysis (section 3) as closely as possible, prescribing a background flow with velocities (U_1, U_2, 0). However, we now impose quadratic drag laws in the uppermost and lowermost layers, consistent with previous analyses of the ice–ocean boundary layer (e.g., McPhee 2012; Cole et al. 2014). Specifically, we prescribe

$$S_1 = -\nabla \times \frac{C_d^{\text{surf}} |\mathbf{u}_1| \mathbf{u}_1}{H_1} + \mathcal{D}_1, \tag{11a}$$

$$S_2 = \mathcal{D}_2, \tag{11b}$$

$$S_3 = -\nabla \times \frac{C_d^{\text{bot}} |\mathbf{u}_3| \mathbf{u}_3}{H_3} + \mathcal{D}_3. \tag{11c}$$

Here we neglect any motion of the overlying sea ice in the prescription of the upper-layer quadratic drag (11a). The additional dissipation terms $\mathcal{D}_i$ in (11a)–(11c) denote dissipation of gridscale enstrophy via spectral truncation. The equations are solved via the same pseudospectral algorithm as used by Arbic et al. (2012), to which the reader is referred for further information of the numerical formulation.

We conduct a series of experiments that span a range of mean flow strengths, upper-ocean shears, and surface drag coefficients, ensuring that we explore a comparable range of interior PV gradients as in Fig. 3. Specifically we covary the upper-layer velocity U_1 over the ranges {1.2, 2.3, 3.5} cm s^{-1}, the upper-ocean shear $U_1 - U_2$ over the range {−1.2, −0.6, 0.0, 0.6, 1.2, 1.7, 2.3, 2.9, 3.5, 4.1, 4.6} cm s^{-1}, and the surface drag coefficient C_d^{surf} over the range {1, 6, 12} × 10^{-3}. This yields a total of 99 experiments, each of which is integrated for 10 years to achieve a statistically steady state. These experiments span PV gradients ranging from $f^{-1}Q_{2y} \approx -7 \times 10^{-6}$ m^{-1} to $f^{-1}Q_{2y} \approx +7 \times 10^{-6}$ m^{-1}. This range includes the magnitude of $f|\nabla q| \approx 1 \times 10^{-6}$ m^{-1} inferred from moorings A and B, which we use as a reference simulation. The bottom drag is held constant and set to $C_d^{\text{bot}} = 2 \times 10^{-3}$, and the layer thicknesses are fixed at $H_1 = 80$ m, $H_2 = 170$ m, and $H_3 = 3750$ m. We use a doubly periodic model domain with dimensions of $L_x \times L_y = 1000$ km × 1000 km, discretized using 512 × 512 Fourier modes, yielding a horizontal grid spacing of approximately 2 km. We selected this configuration because the domain width is many times [$\mathcal{O}(100)$] larger than the first Rossby radius of deformation, allowing quasigeostrophic eddies to develop with minimal self-interaction through the periodic boundaries, and because the grid resolves the Rossby radii of deformation at moderate computational cost.

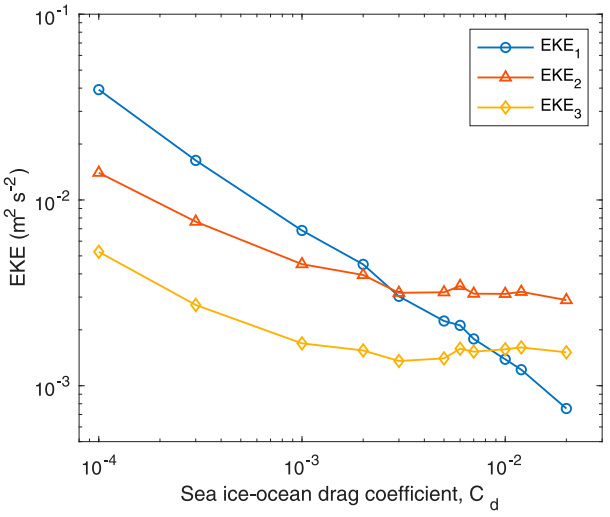

FIG. 4. Dependence of the equilibrated eddy kinetic energy in all three layers of the QG model on the value of the ice–ocean drag coefficient. The simulations were performed for the control experiment, varying only the drag coefficient.

5. Equilibrium eddy field characteristics

Numerical simulations with significantly reduced ice–ocean quadratic drag coefficient produced unrealistically high eddy kinetic energy levels $\mathcal{O}(0.01)$ m^2 s^{-2}, but for a realistic range of drag coefficients ($0.001 \lesssim C_d \lesssim 0.01$) the EKE levels become comparable with observations (Fig. 4). In our framework, the sea ice is considered stationary and the ice–ocean drag coefficient effectively represents a product between the sea ice concentration and the actual ice–ocean drag coefficient; hence, C_d actually changes seasonally but we have neglected this complication. The strong EKE dependence on C_d in all layers (but especially in the surface layer) implies that the ice–ocean damping plays a key role in equilibrating the eddy field, consistent with arguments made in a set of previous studies (e.g., Ou and Gordon 1986; Armitage et al. 2020; Meneghello et al. 2021; Manucharyan and Thompson 2022). We now focus on explaining the sensitivity of eddy length scales and formation mechanisms on the magnitude of the interior PV gradient.

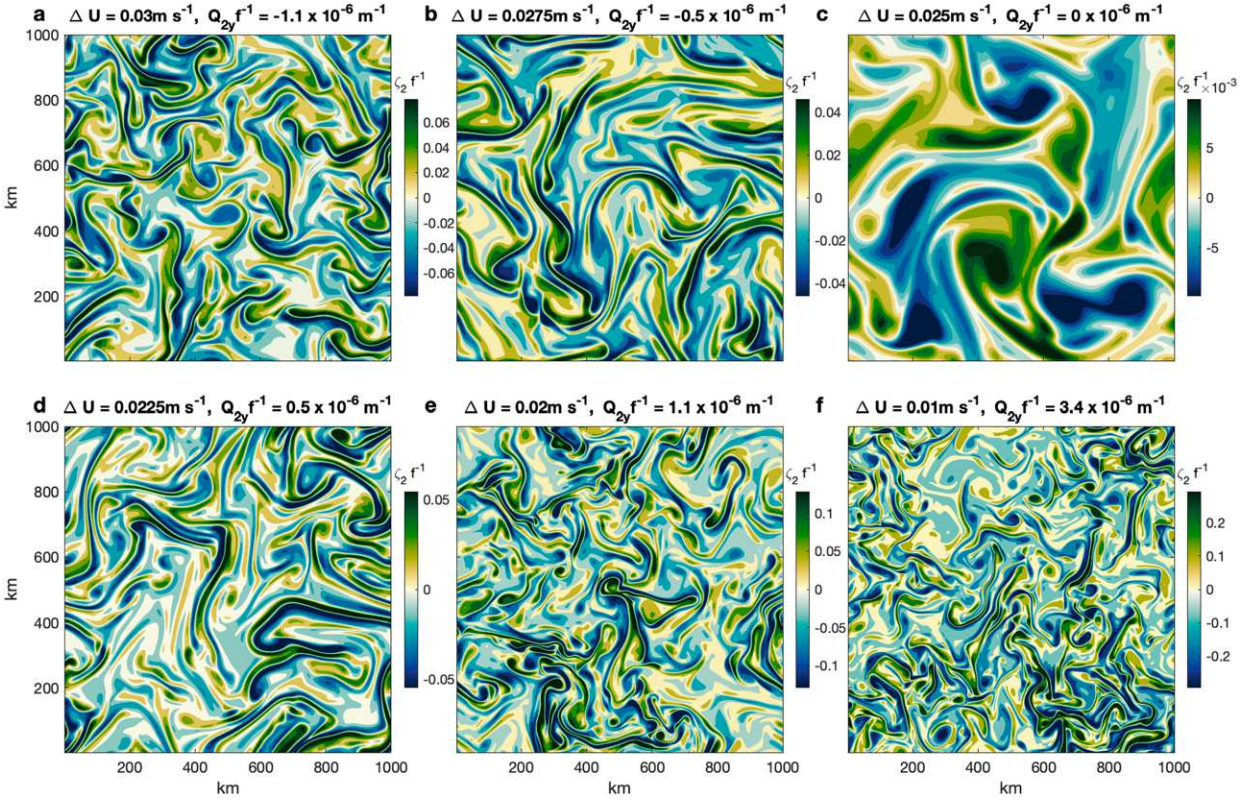

FIG. 5. (a)–(f) A sample of the eddies that manifest across our suite of numerical quasigeostrophic simulations (see section 5). Each panel shows an example of the instantaneous relative vorticity in the middle isopycnal layer in a different simulation, identified by the background shear between the first and second layers (ΔU) and the background PV gradient in the middle layer Q_{2y}. In each case the surface quadratic drag coefficient is $C_d^{\text{surf}} = 6 \times 10^{-3}$ and the top-layer mean flow is $U_1 = 0.03\ \text{m s}^{-1}$. Panel (c) corresponds to the purely Ekman case with zero interior PV gradients; (a) and (b) correspond to an overly weak background flow in the middle layer (relative to the Ekman case), while (d), (e), and (f) correspond to an overly strong subsurface flow.

To elucidate the dependence of the simulated eddy field on the model parameters, and particularly on the interior PV gradient, we first discuss the qualitative features of the flow with reference to representative snapshots of the PV in the middle layer (Fig. 5). Later in this section, we quantify the EKE and eddy length scale dependencies on the interior PV gradient. Eddy activity is visibly minimized in cases with smaller interior PV gradient magnitudes (Figs. 5b,c), corresponding to a purely Ekman-driven flow. In this case the flow is comprised of large-scale wave-like disturbances and filaments that are $\mathcal{O}(100)$ km in size with relative vorticity $\zeta/f \sim \mathcal{O}(0.01)$. As the magnitude of the interior PV gradient increases, the flow develops increasingly energetic small-scale eddies that are typically $\mathcal{O}(30)$ km wide with $\zeta/f \sim \mathcal{O}(1)$, superposed on larger-scale features that are $\mathcal{O}(100)$ km in size. These smaller-scale eddies are typically subsurface intensified, i.e., their flow is largely confined to the middle isopycnal layer. In Fig. 6 we illustrate this vertical structure via a transect across specimen cyclonic and anticyclonic eddies, taken from a snapshot of one of our simulations with a relatively strong interior PV gradient of $f|\nabla q| = 1 \times 10^{-6}\ \text{m}^{-1}$. Within the anticyclonic (cyclonic) eddy, the upper isopycnal interface domes up (down) while the lower isopycnal interface domes down (up).

The emergence of smaller-scale eddies in simulations that impose stronger interior PV gradients is superficially consistent with the appearance of higher-wavenumber unstable modes in our linear stability analysis (Figs. 3a,b). To refine this comparison we now quantify the dependence of the eddy energy and length scales on the interior PV gradient. In Fig. 7b we plot the area-averaged eddy kinetic energy (EKE),

$$\text{EKE}_i = \frac{1}{2}(u_i^2 + v_i^2), \tag{12}$$

in each member of our suite of nonlinear simulations. Similarly, in Fig. 7a we plot the dominant eddy length scales $\lambda_{\text{eddy},i}$, defined as the length scale over which the meridional autocorrelation of the meridional velocity drops by a factor of e. Figure 7b shows that the EKE density in the middle layer almost always exceeds that in the upper and lower layers, except when the interior PV gradient is very close to zero ($|\partial_y Q_2/f| \lesssim 10^{-3}\ \text{km}^{-1}$). Figure 7a shows that the energy in the middle layer is dominated by relatively small scales of ~30 km, while the energy in the upper and lower layers is contained at much larger scales of ~80 km and $\gtrsim$100 km, respectively. The exception occurs close to $\partial Q_y = 0$, where all three layers exhibit eddy length scales of ~150 km.

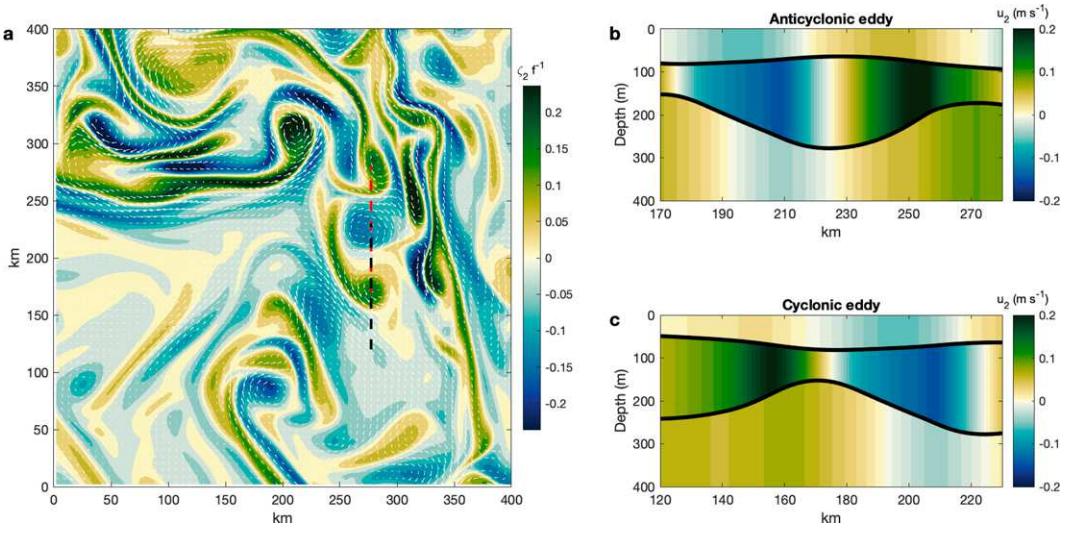

FIG. 6. Vertical and horizontal structure of specimen subsurface-intensified cyclonic and anticyclonic eddies in a reference simulation (shown in Fig. 5e). (a) Snapshot of the relative vorticity in the middle isopycnal layer. White arrows denote the velocity in the middle layer; for clarity, only every third velocity vector is plotted. The red and black dashed lines identify the specimen subsurface-intensified anticyclonic and cyclonic eddies and indicates the location of the transect shown in (b) and (c). (b),(c) Transects of the zonal velocity across the specimen subsurface-intensified eddies, black curves denoting the interfaces between the three isopycnal layers.

Taken together, these diagnostics indicate that interior PV gradients produce a small-scale, subsurface-intensified eddy field. When the interior PV gradient becomes sufficiently weak, corresponding to the limit of a purely Ekman-driven flow, the eddy field becomes orders of magnitude weaker and dominated by much larger, approximately barotropic structures. The length scales of the large and small eddies in our simulations (Fig. 7a) are approximately consistent with the scales of the two unstable mode branches in our linear stability calculations (Fig. 3d). However, the high-wavenumber instability branch (see Fig. 3a) vanishes across almost the entire range of PV gradients explored in our simulations (Fig. 5) and observed in nature (Fig. 1a). This suggests that the generation of the small, subsurface-intensified eddies results from a nonlinear mechanism, which we explore in section 6. We note, however, that a comparison of eddy characteristics between sparse observations and our idealized model simulation is imperfect as it relies on values found in the literature that use different methods.

6. Formation mechanism of subsurface-intensified eddies

In section 5 we showed that the generation of subsurface-intensified eddies in nonlinear quasigeostrophic simulations differs substantially from the predictions of linear stability theory (section 3). We now show that this difference occurs because the subsurface-intensified eddies are generated by barotropic eddy stirring of PV anomalies in the interior isopycnal layer.

We first provide a visual illustration of the mechanism via which subsurface-intensified eddies are generated, shown in Fig. 8. Here we have initialized a simulation using a "smoothed" snapshot from the experiment shown in Fig. 5e. We selected this simulation because the background PV gradient $Q_{2y}/f_0 = 10^{-6}\ \mathrm{m}^{-1}$ is comparable to those diagnosed in the Beaufort Gyre from the MIMOC climatology and estimated from moorings A and B (note, moorings C and D have much weaker interior PV gradients). The smoothing is performed by removing variations in the PV at wavelengths smaller than 200 km, and serves to remove the subsurface-intensified eddies from the PV snapshot. Figure 8 shows the evolution of the second-layer relative vorticity field over 140 days of this experiment, and visualizes the reemergence of the small-scale (30–50 km) subsurface-intensified eddies. Within ~20 days (Fig. 8a, advection by the larger-scale flow has already created PV gradients scales of $\mathcal{O}(10)$ km. By $t = 40$ days (Fig. 8b), these gradients are visibly beginning to destabilize and form small-scale vortices. These small-scale vortex formation events become increasingly numerous at $t = 60$ and $t = 80$ days (Figs. 8c,d). By $t = 100$–120 days (Figs. 8e,f), small-scale eddies are ubiquitous, and their formation process can no longer be visually distinguished from the ambient eddy field.

To complement the visual illustration provided by Fig. 8, we now provide quantitative evidence that barotropic advection of interior PV anomalies is responsible for generating the subsurface-intensified eddies. Specifically, we decompose the flow in our numerical experiments into baroclinic modes and quantify the transfer of enstrophy between modes. The baroclinic mode decomposition is described in detail in the appendix, and follows the approach of Smith and Vallis (2001). Briefly, the baroclinic modes of our three-layer system are defined by the eigenvectors $\mathbf{e}_m$, $m = 1, \ldots, 3$ of the vertical quasi-differential operator on the right-hand sides of (4a)–(4c). These eigenvectors

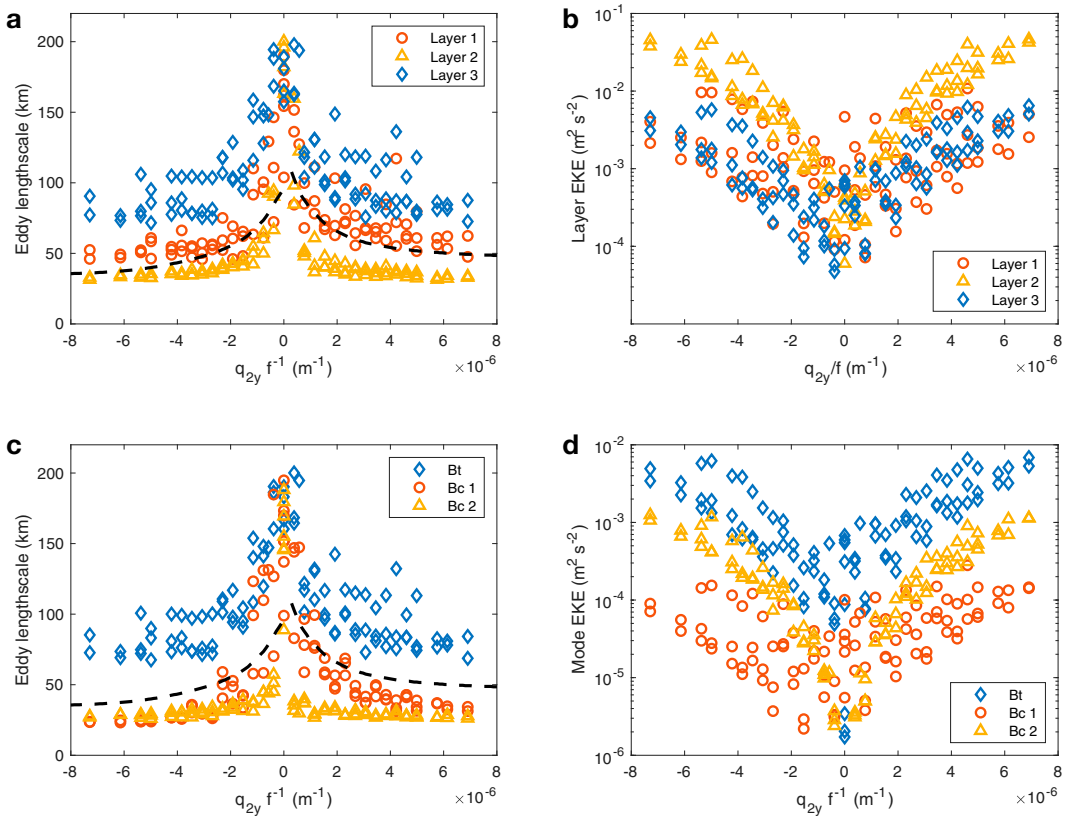

FIG. 7. Dependence of the eddy characteristics on the interior PV gradient. (a),(c) Eddy length scales and (b),(d) eddy kinetic energy partitioning in different (top) isopycnal layers and (bottom) barotropic/baroclinic modes (see sections 5 and 6 for definitions). Each point corresponds to one member of our suite of numerical experiments, and all quantities are averaged in time and over the entire model domain in each experiment. Colored points in (a) and (b) correspond to the top-layer diagnostics, while in (c) and (d) they correspond to vertical modes. Note, there is a significant scatter in data points as the interior PV gradient is not the only parameter that changes between the simulations.

comprise an orthogonal basis for the vertical structure of any variable in our three-layer system. For example the instantaneous PV vector $\mathbf{q}(\mathbf{x}, t) = \{q_k, k = 1, \ldots, 3\}$, can then be uniquely written as a linear combination of the modal structures,

$$\mathbf{q}(\mathbf{x}, t) = \sum_{m=1}^{3} \hat{q}_m(\mathbf{x}, t)\mathbf{e}_m, \tag{13}$$

where $\hat{q}_m$ is the amplitude of the mth mode. Figure 9 illustrates the structures of the three baroclinic modes in our model: the barotropic, first baroclinic, and second baroclinic modes. We will interchange the subscripts 1, 2, and 3 with bt, bc1, and bc2 for clarity.

Figure 9 suggests that there should be a close correspondence between the barotropic, first-baroclinic, and second-baroclinic modes and the flows in layers 3, 1, and 2, respectively. To test this, we compute the energy in each baroclinic mode, averaged over the full depth of the water column. Figure 7d shows that the energy in the modes exhibits a qualitatively similar dependence on $\partial_y Q_2$ as the energy in the layers: the EKE is lowest for $f^{-1}Q_{2y} = 0$, and increases by two orders of magnitude when $|f^{-1}Q_{2y}|$ is comparable to the PV gradient estimated from moorings A and B (5×10^{-6} m^{-1}), with approximate symmetry for positive and negative $f^{-1}Q_{2y}$. However, the magnitudes differ because the modal energies are computed over the full water column depth, which emphasizes the flow in the deep, bottom layer, which is dominated by the barotropic mode. We also compute the dominant length scales of the flow associated with each baroclinic mode following the same approach as described in section 5, but using autocorrelations of $\hat{v}_{\mathrm{bt}}$, $\hat{v}_{\mathrm{bc1}}$, and $\hat{v}_{\mathrm{bc2}}$, rather than v_1, v_2, and v_3. Figure 7c confirms that the barotropic mode is dominated by large length scales, decreasing from ~150 km when the middle-layer PV gradient $\partial_y Q_2$ is close to zero, to ~100 km for sufficiently large $|\partial_y Q_2|$. This is similar to the length scale dependence of the flow in layer 3. However, the second baroclinic mode is consistently dominated by smaller length scales of ~30–40 km, whereas the flow in layer 2 exhibits larger length scales when $\partial_y Q_2$ is close to zero; this is consistent with the approximate vanishing of the second-mode energy as $\partial_y Q_2 \to 0$ (Fig. 7b). The dependence of the first baroclinic mode on $\partial_y Q_2$ qualitatively resembles that of the flow in layer 1, but the length scales approach those of the second baroclinic mode for sufficiently large $\partial_y Q_2$.

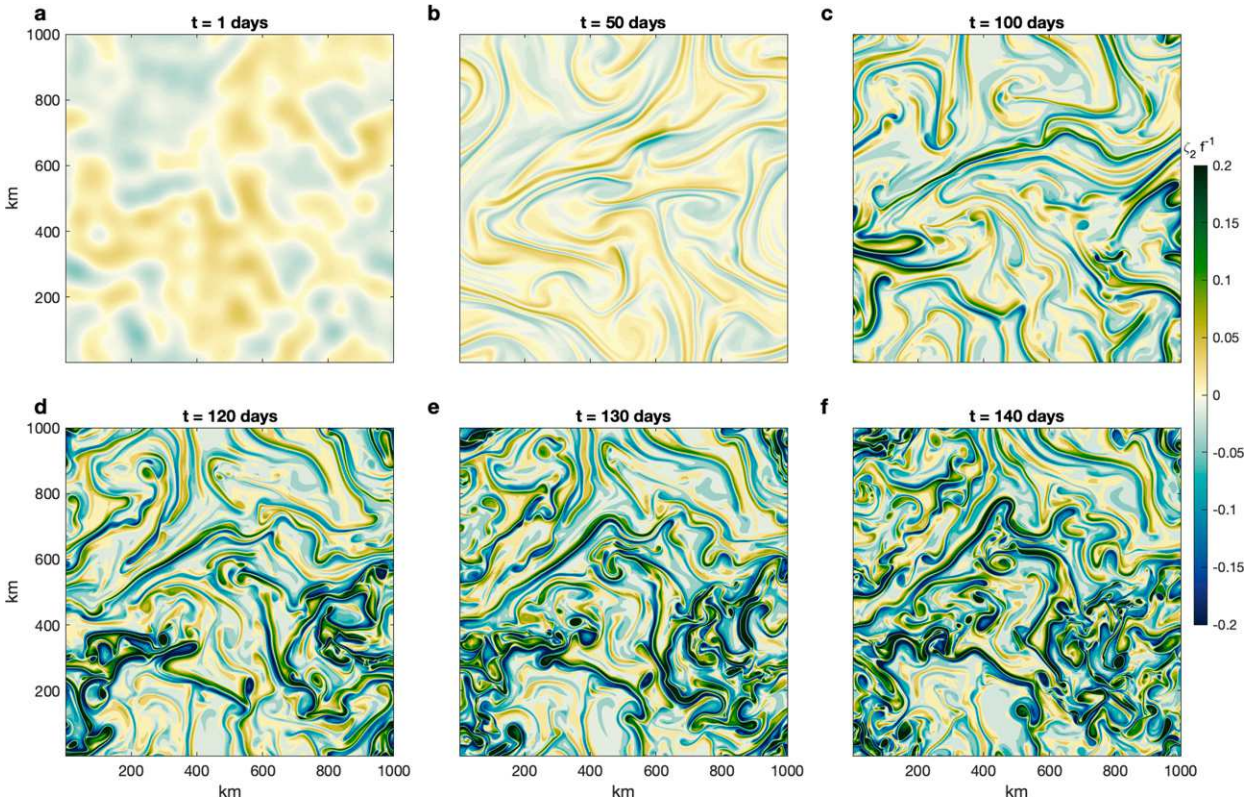

FIG. 8. Emergence of small-scale, subsurface-intensified eddies due to stirring of interior PV gradients by large-scale, barotropic eddies. This simulation was initialized using a filtered snapshot from the simulation shown Fig. 5e, preserving only flows with scales larger than 100 km. The panels show snapshots of the relative vorticity in the middle isopycnal layer; the panel titles denote the time since the beginning of the simulation.

We now quantify the generation of second-mode eddies using the enstrophy budget, decomposed into baroclinic modes. We use the enstrophy budget instead of the energy budget because the conversions between the mean and eddy enstrophy reservoirs are mathematically simpler. The derivation of the modal enstrophy budget, decomposed into mean and eddy components, is given in the appendix. Briefly, we first note that the depth-integrated enstrophy can be decomposed exactly

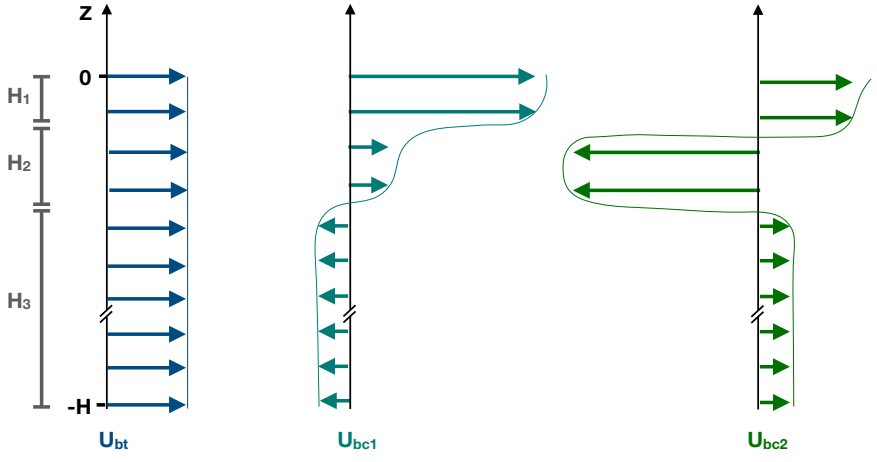

FIG. 9. Profiles of the barotropic and the two baroclinic modes in the three-layer quasigeostrophic model. The arrow sizes match quantitatively with the vertical modes: (3.3, 0.7, −0.1) $km^{-0.5}$ for the first baroclinic mode and (1.1, −2.3, 0.08) $km^{-0.5}$ for the second baroclinic mode; the modes have been normalized to have the norm of 1. Note the axis breaks within the third layer, which is much deeper than the first two.

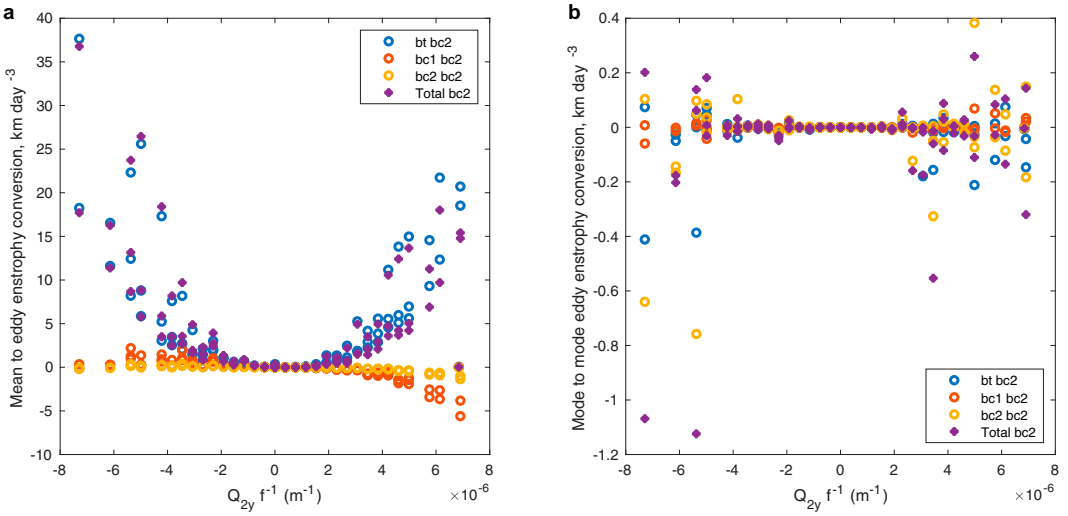

FIG. 10. Quantification of the sources and sinks of enstrophy in the second baroclinic mode, $\langle (1/2)\hat{q}_{\mathrm{bc}}^2 \rangle$ [see Eq. (14)]. For each of our suites of numerical quasigeostrophic experiments (see section 5), we plot the area- and time-averaged (a) mean-to-eddy enstrophy conversion and (b) eddy-to-eddy enstrophy conversion (purple points). In (a) we additionally show 3 of the 9 modal mean-to-eddy enstrophy conversion terms, associated with barotropic advection of second mode PV anomalies ($\sim\langle \hat{v}_{\mathrm{bt}}\hat{q}_{\mathrm{bc2}}\rangle \partial_y \hat{Q}_{\mathrm{bc2}}$, blue points), first mode advection of second mode PV anomalies ($\sim\langle \hat{v}_{\mathrm{bc1}}\hat{q}_{\mathrm{bc2}}\rangle \partial_y \hat{Q}_{\mathrm{bc2}}$, red points), and second mode advection of second mode PV anomalies ($\sim\langle \hat{v}_{\mathrm{bc2}}\hat{q}_{\mathrm{bc2}}\rangle \partial_y \hat{Q}_{\mathrm{bc2}}$, yellow points). In (b) we similarly show 3 of the 9 modal eddy-to-eddy enstrophy conversion terms, associated with barotropic advection of second mode PV anomalies ($\sim\langle \hat{\mathbf{u}}_{\mathrm{bt}}\hat{q}_{\mathrm{bc2}} \cdot \nabla \hat{q}_{\mathrm{bc2}}\rangle$, blue points), first mode advection of second mode PV anomalies ($\sim\langle \hat{\mathbf{u}}_{\mathrm{bc1}}\hat{q}_{\mathrm{bc2}} \cdot \nabla \hat{q}_{\mathrm{bc2}}\rangle$, red points), and second mode advection of second mode PV anomalies ($\sim\langle \hat{\mathbf{u}}_{\mathrm{bc2}}\hat{q}_{\mathrm{bc2}} \cdot \nabla \hat{q}_{\mathrm{bc2}}\rangle$, yellow points).

into positive-definite contributions from the enstrophies in each baroclinic mode, $(1/2)\hat{q}_m^2$, $m = \mathrm{bt}, \mathrm{bc1}, \mathrm{bc2}$. The domain-integrated modal enstrophies satisfy an evolution equation of the form

$$\partial_t \left\langle \frac{1}{2}\hat{q}_n^2 \right\rangle = \underbrace{-\sum_m \sum_l \langle \hat{v}_m \hat{q}_l \rangle \partial_y \hat{Q}_n \varepsilon_{mln}}_{\text{mean-to-eddy enstrophy conversion}} + \underbrace{\sum_m \sum_l \langle \hat{\mathbf{u}}_m \hat{q}_l \cdot \nabla \hat{q}_n \rangle \varepsilon_{mln}}_{\text{mode-to-mode eddy enstrophy transfer}} + \underbrace{\langle \hat{\mathcal{D}}_n \hat{q}_n \rangle}_{\text{enstrophy dissipation}}, \tag{14}$$

where the angle brackets denote an integral over the model domain and an average in time

$$\langle \cdot \rangle = \iint_A dA \frac{1}{T} \int_{t_0}^{t_0+T} dt. \tag{15}$$

The mean-to-eddy enstrophy conversion term in (14) quantifies the production of eddy enstrophy in each mode, which results from advection of PV anomalies ($\langle \hat{v}_m \hat{q}_l \rangle$) down the corresponding mean modal PV gradient ($\partial_y \hat{Q}_n$). Importantly, the advection of PV anomalies can occur due to any combination of modes, i.e., enstrophy in mode n can be produced by the velocity in any mode m advecting PV anomalies in any mode l. The mode-to-mode eddy enstrophy transfer is structured similarly, but results from triple correlations between modal velocity anomalies, PV anomalies, and PV gradient anomalies. Both of these terms are proportional to the mode interaction coefficient,

$$\varepsilon_{mln} \equiv \sum_k H_k e_{mk} e_{lk} e_{nk}. \tag{16}$$

Note that $\boldsymbol{\varepsilon}_{mln}$ is not the Levi–Civita symbol; it is simply a matrix whose entries are equal to the vertical integrals of cubic products of the baroclinic modal eigenvectors.

In Fig. 10 we plot the domain-integrated mean-to-eddy enstrophy conversion and eddy-to-eddy enstrophy transfer to the second baroclinic mode [i.e., to $\langle (1/2)\hat{q}_{\mathrm{bc2}}^2 \rangle$] from (14), in our suite of numerical simulations. These plots show that mean-to-eddy enstrophy conversion is consistently a source of second-mode eddy enstrophy, and is typically an order of magnitude larger than the eddy-to-eddy enstrophy transfer. This implies that the primary balance in the second-mode enstrophy budget (14) is between mean-to-eddy enstrophy conversion and enstrophy dissipation, though we do not quantify the latter directly. Furthermore, Fig. 10a shows that the mean-to-eddy enstrophy transfer is consistently dominated by a single term, corresponding to barotropic advection of second-mode PV anomalies, or $\langle \hat{v}_{\mathrm{bt}}\hat{q}_{\mathrm{bc2}} \rangle \cdot \partial_y \hat{Q}_{\mathrm{bc2}} \cdot \varepsilon_{\mathrm{bt,bc2,bc2}}$. This finding supports the mechanism suggested by Fig. 8: the second-mode, or subsurface-intensified, eddies are generated via advection of interior PV anomalies by larger-scale, approximately barotropic eddies.

Finally, we develop a scaling to synthesize our qualitative illustration and enstrophy budged-based quantification of the

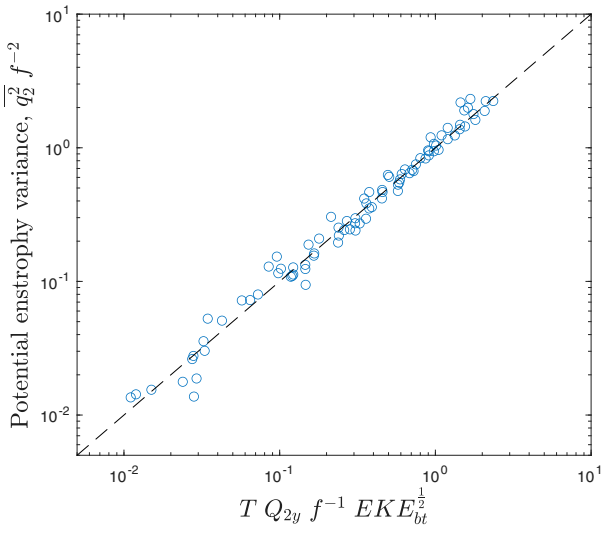

FIG. 11. Test of our scaling for the subsurface eddy enstrophy, Eq. (19). Each point corresponds to one member of our suite of numerical quasigeostrophic experiments (see section 5), and each term in the scaling is averaged in time and over the entire model domain. A single parameter fit was performed with the best-fit value of the time scale $T = 24$ days.

subsurface-intensified eddy generation mechanism. Given the close correspondence between the flow in the middle isopycnal layer and in the second baroclinic mode (Fig. 7), and given that the production of second-mode enstrophy is approximately proportional to $\langle \hat{v}_{\rm bt}\hat{q}_{\rm bc}\rangle \cdot \partial_y \hat{Q}_{\rm bc2}$, we pose an approximate scaling for the second-layer enstrophy budget as

$$\partial_t q_2^2 \sim v_{\rm bt} q_2 \partial_y Q_2 - \mathcal{C}_{\rm diss} q_2^p. \tag{17}$$

Here we have posited that the dissipation of second-layer enstrophy scales with q_2 raised to an unknown power p, with an unknown coefficient $\mathcal{C}_{\rm diss}$. To further simplify (17), we assume steady state ($\partial_t \approx 0$), we assume that the magnitude of the barotropic flow scales with the barotropic eddy kinetic energy, $v_{\rm bt} \sim {\rm EKE}_{\rm bt}^{1/2}$, and we assume second-layer PV anomalies scale with the second-layer eddy enstrophy, $q_2 \sim Z_2^{1/2} = \langle (1/2) q_2^2 \rangle^{1/2}$. Making these substitutions in (17) and rearranging, we obtain

$$Z_2^{(p-1)/2} \sim {\rm EKE}_{\rm bt}^{1/2} \partial_y Q_2. \tag{18}$$

Empirically, we find that this scaling most closely matches our numerical simulations when the enstrophy dissipation scales as $Z_2^{3/2}$, i.e., for $p = 3$. In this case (18) reduces to

$$Z_2 \sim {\rm EKE}_{\rm bt}^{1/2} \partial_y Q_2. \tag{19}$$

In Fig. 11 we show that (19) agrees closely with diagnostics from our suite of numerical simulations across two orders of magnitude in Z_2. This lends additional support to our finding that the smaller, subsurface-intensified eddies are generated by advection of interior PV anomalies by the larger-scale, approximately barotropic eddies. The coefficient of proportionality in Fig. 11 is a time scale $T \approx 24$ days, which may be interpreted as the time scale for the second mode enstrophy to be removed by gridscale dissipation.

7. Summary and discussion

Previous studies have shown that the Beaufort Gyre hosts a wide range of eddies. The eddies that clearly stand out from the background conditions appear in mooring and ITP data as high-Rossby-number localized coherent vortices with cores residing in the interior of the water column (e.g., Zhao et al. 2014, 2016). These eddies are thought to be generated remotely at the continental slope currents and propagated into the interior of the gyre (Hunkins 1974; D'Asaro 1988; Zhao et al. 2014). In this paper, we point out that the baroclinic instability of interior BG currents could generate a different type of eddies, characterized by large length scales, about 50–100 km, and low Rossby numbers, $\mathcal{O}(0.1)$. These large-scale eddies are consistent with recent satellite observations that indicate the frequent eddy appearance with diameters of 60 km (Kozlov et al. 2019; Kubryakov et al. 2021; Manucharyan et al. 2022), but they have not yet been comprehensively explored using in situ observations in which the strong localized vertices appear dominant (Zhao et al. 2014, 2016). The existence of large-scale eddies was rationalized by the idealized eddy-resolving simulations of Manucharyan and Spall (2016) in a context of such eddies being necessary to generate the eddy overturning that could counteract the Ekman pumping-induced vertical velocity and contribute to BG equilibration. However, in this and following idealized simulations (Meneghello et al. 2018a; Spall 2020), the eddy length scales are greater than 100 km, appearing to be overly large compared to available satellite observations.

a. Summary of key findings

In this study, we highlighted the critical role of interior PV gradients in energizing and diminishing the length scales of large mesoscale eddies formed by the instabilities of interior BG currents. Specifically, we demonstrated that the background velocity profiles associated solely with the Ekman-driven vertical displacement of isopycnals only generate relatively weak eddies substantially larger than 100 km. These eddies form as a result of a direct baroclinic instability of the mean flow with no interior PV gradients (the Eady problem) that involves resonant interactions between the surface and the abyssal ocean layers (section 3). The emerging eddies are surface intensified, consisting predominantly of the barotropic and the first baroclinic modes (e.g., Figs. 3 and 5c). However, based on the analysis of mooring observations and climatological BG state, its large-scale currents contain substantial interior PV gradients in the Pacific halocline layer that lead to dramatic changes in eddy scales derived from the linear stability analysis and observed in nonlinear instability simulations.

Using a set of idealized simulations, in sections 5 and 6 we reveal a formation mechanism for the subsurface-amplified eddies with length scales significantly smaller than those expected from the linear stability of the mean flow (see Fig. 6). The large-scale eddies stir the PV gradients in the interior of the halocline and generate filamentary structures that advect

the weak interior PV gradients over large distances (Fig. 8). This resulting localized PV filaments then become unstable and form smaller-scale subsurface-intensified eddies, with diameters on the order of 40 km and smaller and Rossby numbers of $\mathcal{O}(0.1)$ and higher. The observed velocity profiles in the BG moorings (Fig. 2) are consistent with relatively strong interior PV gradients ($Q_{2y}f^{-1}$ of up to 1×10^{-6} m^{-1}) at moorings A and B, while relatively weak interior PV gradients appear at moorings C and D. This suggests that the eddy stirring mechanism that generates the subsurface-amplified eddies should be spatially heterogeneous and likely prominent at the locations of moorings A and B. In contrast, the climatologically derived PV gradients have similar magnitudes at all four mooring locations but averaged over the BG interior $Q_{2y}f^{-1} \approx 0.4 \times 40^{-6}$ m^{-1}, which is significantly smaller than that estimated from velocity observations in moorings A and B but higher than for moorings C and D. This suggest that subsurface-intensified eddy activity could be highly heterogeneous in space, spanning a range of scenarios shown in Fig. 5.

Note that the QG simulations corresponding to a particular value of the PV gradient would likely provide an overestimated eddy energy because they use a uniform PV gradient over an entire 1000 km $\times$ 1000 km simulation domain while the high PV gradients in moorings are likely representative of a smaller surrounding area. Nonetheless, the representative QG simulation with $Q_{2y}f^{-1} = 10^{-6}$ m^{-1} results in the $\mathcal{O}(5 \times 10^{-3})$ m^2 s^{-2} mean eddy kinetic energy in the second layer, which is similar to the energy levels reflected by the moorings. This implies that the PV stirring mechanism can substantially energize the BG eddy field, and hence to better simulate the eddy field in eddy-resolving ocean models, it may be necessary to pay close attention to how well they represent the mean interior PV gradients. We also note the similarity between the discussed PV stirring mechanism and the submesoscale eddy formation via advection of mixed layer density gradients by a mesoscale strain that can also lead to filamentation and secondary instabilities (Thomas et al. 2008; McWilliams 2016). Since our discussed mechanism is sufficiently general, it could be active in other ocean regions as long as the PV there is not completely homogenized and there are mechanisms to energize large-scale eddies with a significant barotropic signal.

Eddies of various sizes participate in the energy and enstrophy cascades, resulting in the equilibrium eddy field that becomes more energetic and contains smaller scales with increasing interior PV gradients (Fig. 7). Analyzing the interactions between the different baroclinic modes, we identified that it is specifically the barotropic mode stirring of the interior PV gradients that transfers the enstrophy into the interior layer (Fig. 10). Based on this barotropic stirring mechanism, we proposed a scaling law in which the interior enstrophy is directly proportional to the background PV gradient in that layer and the square root of the barotropic eddy kinetic energy (Fig. 11). The scaling law is accurate across a wide range of mean flow profiles and surface drag coefficients, with only a single fitting time scale parameter $T \approx 24$ days. The exact interpretation of this parameter remains unclear, but it can be speculated that its magnitude is related to the dissipation of enstrophy in the middle layer, which in our model is achieved with spectral filtering akin to hyperviscosity. In nature, the enstrophy destruction in the interior of the Beaufort Gyre is likely governed by small-scale nongeostrophic processes such as lateral intrusions and vertical mixing.

b. *Caveats and outlook for future research*

Several idealizations in our study can qualitatively affect the interpretation of the observed eddy characteristics. Most notable is the representation of the continuously stratified ocean with only three quasigeostrophic layers and the use of the spatially homogeneous and stationary background mean flow. The three-layer system allows only the development of the barotropic and the two baroclinic modes as the interior eddies occupy the entire Pacific winter halocline. Zhao et al. (2018) have shown that kinetic energy in the Beaufort Gyre is indeed concentrated in the barotropic and first two baroclinic modes. However, if multiple layers are used with the Pacific halocline layer, even smaller eddies with higher Rossby numbers could potentially form via the same stirring mechanism or due to the emergence of additional instability modes associated with PV reversals within the halocline layer, as was argued in Meneghello et al. (2021). In this case, one could expect the enstrophy transfer in the interior layers to depend not only on the barotropic mode but also on the second (or higher) baroclinic mode, i.e., the 40–100-km eddies discussed in our simulations could also stir the PV gradients within the halocline and contribute to the generation of even smaller-scale eddies that would occupy only a fraction of the Pacific halocline layer. Such smaller-scale eddies might resemble the intrahalocline and sub–mixed layer eddies observed in ITPs and moorings, which typically have length scales of $\mathcal{O}(10)$ km and Rossby numbers of $\mathcal{O}(1)$.

An associated caveat is that the temperature and salinity signatures of the observed small-scale eddies, which are predominantly anticyclonic with cores localized within the halocline layer, suggest a remote formation mechanism (Hunkins 1974; Manley and Hunkins 1985; Zhao et al. 2014) instead of the local instability. Exploring the remote formation of anticyclones at the slope currents and their subsequent propagation to the BG interior, Spall et al. (2008) notes that these eddies have lifetimes of about 2 years, during which they are effective in carrying water mass properties with them. Hence, it is possible that the water mass transfer by those remotely formed eddies is creating the observed interior PV gradients necessary for our proposed stirring mechanism of eddy generation. A more detailed analysis of the observations is needed to better understand the complexities of the BG eddy dynamics.

Our simulations demonstrate that for the eddy field to equilibrate to a realistic range of energies and Rossby numbers, the existence of a quadratic surface drag associated with the sea ice cover is strictly necessary (Fig. 4). The winter sea ice moves slowly compared to the eddy velocities simulated here (Spreen et al. 2011; Holland and Kwok 2012), and hence primarily acts as a lid that drains the eddy kinetic energy,

favoring subsurface-intensified eddies over surface-intensified eddies. Without sea ice, the primary mechanism of energy dissipation is absent and the eddy field becomes an order of magnitude more energetic, provided the mean flow stays the same. While our study considered constant-in-time drag coefficients, the strong seasonality in surface dissipation of eddies might lead to significant seasonality in eddy dynamics, and with the increasingly larger areas of the Beaufort Gyre becoming seasonally ice-free (Cavalieri and Parkinson 2012; Serreze and Stroeve 2015) the eddy field is expected to be more energetic (Armitage et al. 2020; Manucharyan et al. 2022). Note that current eddy parameterizations used in coarse-resolution climate models have been developed for ice-free oceans and do not take sea ice into account, and recently sea ice–aware parameterizations of submesoscale eddies have been proposed (Shrestha and Manucharyan 2022).

Our other idealization is the use of the spatially heterogeneous and stationary background flow, which allowed us to explore a wide range of mean flow configurations. In reality, however, the background currents are not stationary and the associated PV gradients are spatially heterogeneous (Fig. 1a). The localized nature of the currents, particularly near bathymetric features, affects their stability characteristics because, in addition to the baroclinic instabilities examined in section 3, the horizontal shear can introduce barotropic and mixed instabilities. Meanwhile, the topographic beta effect can act to either suppress or amplify the instabilities depending on the relative orientation of the isopycnal and bathymetric slopes (Blumsack and Gierasch 1972; Isachsen 2011). The impact of these lateral heterogeneities on the generation of subsurface-intensified Arctic eddies remains to be explored.

Comprehensive eddy-resolving ocean models present an alternative approach to exploring BG eddy generation mechanisms, but our findings suggest that it is necessary for such models to generate a realistic stratification and mean flow with correct interior PV gradients. For instance, the high-resolution simulations of Regan et al. (2020) and Wang et al. (2020) significantly underestimate the EKE in the BG interior (see section 1). The results of our study imply that the lack of EKE in eddy-resolving models may be due to the overly weak interior PV gradients and/or overly weak barotropic eddies [see Eq. (19)]. It is also possible that the remotely formed eddies in those models are not propagating toward the BG interior fast enough given their lifetimes and hence do not contribute to the interior EKE.

c. Conclusions

In summary, our study demonstrates that advection of interior PV gradients by relatively large-scale eddies with a barotropic flow component could be the key formation mechanism of mesoscale eddies that are about 40–100 km in diameter and localized in the interior of the BG halocline. These large-scale and low Rossby number eddies have not been characterized in the Beaufort Gyre because the attention of the observational community has been drawn to more energetic and localized small-scales eddies with remote formation mechanisms (Hunkins 1974; Manley and Hunkins 1985; Zhao et al. 2014, 2016). However, the remotely formed eddies that decay weakly as they propagate to the interior of the gyre are not expected to significantly contribute to the eddy overturning streamfunction as the isopycnal eddy thickness (or PV) fluxes are strongest only near their formation sites [see the nonacceleration result in Vallis (2017)].

Thus, only the large-scale eddies are expected to drive the eddy overturning and counteract the Eulerian mean vertical velocity in the BG because they form as a direct result of local baroclinic instabilities of the BG currents. The large eddies may also be efficient in transporting water parcels and biogeochemical tracers over large distances, as they are more coherent over large distances compared to small-scale isolated eddies. Nonetheless, it is important to note that the different types of eddies actively interact with the mean flow as well as with each other via the energy and enstrophy cascades, and hence separating their roles in the Beaufort Gyre dynamics is a challenging problem.

Given the importance of the interior PV gradient in defining the BG eddy characteristics, it is crucial to understand the processes that create it and accurately represent those in numerical models and theory. Note that Ekman pumping for an f-plane gyre leads to nearly parallel deepening of all isopycnals in the interior of the water column and thus cannot generate PV gradients in those isopycnal layers that do not outcrop at the location where that pumping occurs (see section 2). However, exploring the vertical structure of the BG halocline and its transient response to Ekman pumping, Kenigson et al. (2021) demonstrate that as the gyre spins up (spins down), the halocline thickness gradient in the Pacific layer increases (decreases). This behavior can be caused by mesoscale eddies if they act according to the Gent–McWilliams parameterization with depth-dependent diffusivity rather than an assumption of eddy PV diffusion.

Assuming this is indeed the case, a complex picture of the Ekman-driven eddy dynamics emerges. The Ekman pumping generates geostrophic flows with zero interior PV gradients, but those flows are nonetheless baroclinically unstable and form weak large-scale eddies. These eddies cumulatively act to generate the interior PV gradients, i.e., they result in an antidiffusive process with the isopycnal thickness flux directed from the boundaries, where the isopycnal layer thickness is smaller, toward the center of the gyre, where the thickness is larger. However, antidiffusive eddy processes are counterintuitive and need systematic exposition. It is also possible that the interior PV gradients are generated due to the offshore water mass transport by small-scale eddies formed at the slope currents. In either case, the presence of the interior PV gradient leads to the amplification of the eddy growth rates, reduction of their length scales from about 200 to 40 km, and a dramatic enhancement of the eddy kinetic energy in the Pacific halocline layer. The equilibrium is presumably established when the interior eddies counteract the buildup of the interior PV gradients. Understanding the response of such complex eddy–mean flow interactions to changes in the winds, sea ice cover, and resulting Ekman pumping would require comprehensive eddy field observations and accurate representation of the interior PV gradients and associated instabilities in ocean models.

Acknowledgments. ALS and GEM were supported by the National Science Foundation under Grants OCE-1751386 and OCE-1829969, respectively. The authors thank Glenn Flierl for providing the basic quasi-geostrophic model code that was adapted to perform the nonlinear simulations in this study. Finally, the authors thank the four reviewers and the editor for their valuable critique of the manuscript.

Data availability statement. The mooring data used in this study were collected and made available by the Beaufort Gyre Exploration Program based at the Woods Hole Oceanographic Institution (https://www.whoi.edu/beaufortgyre) in collaboration with researchers from Fisheries and Oceans Canada at the Institute of Ocean Sciences. A global monthly isopycnal upper-ocean climatology with mixed layers (MIMOC) is available from https://www.pmel.noaa.gov/mimoc/.

APPENDIX

Mean/Eddy Enstrophy Budget Decomposed into Baroclinic Modes

In this appendix, we derive a decomposition of the QG enstrophy budget into mean and eddy components of the flow and into baroclinic modes. We use this budget to quantify the sources of enstrophy in the second baroclinic mode and to motivate a scaling relation for the enstrophy in this mode. The derivation follows a similar approach as that of Smith and Vallis (2001) for the baroclinic modal decomposition of the energy budget. We first derive the budget equations for an arbitrary number of layers and baroclinic modes, then specialize the equations to the configuration of our QG model equations in the main text, in which the direction of the PV gradient does not vary with depth.

The QG evolution equations describe conservation of PV,

$$\frac{\partial q_k}{\partial t} + \mathbf{u}_k \cdot \nabla q_k = \mathcal{D}_k, \tag{A1}$$

where q_k, $\mathbf{u}_k$, and $\mathcal{D}_k$ denote the PV, horizontal velocity, and nonconservative terms in each layer, respectively, for $k = 1, \ldots, N$. The PV in each layer is given by (Vallis 2017)

$$q_1 = \beta y + \nabla^2 \psi_1 + \frac{f_0^2}{H_1}\left(\frac{\psi_2 - \psi_1}{g'_{3/2}}\right), \tag{A2a}$$

$$q_k = \beta y + \nabla^2 \psi_k + \frac{f_0^2}{H_k}\left(\frac{\psi_{k-1} - \psi_k}{g'_{k-1/2}} - \frac{\psi_k - \psi_{k+1}}{g'_{k+1/2}}\right), \tag{A2b}$$

$$q_N = \beta y + \nabla^2 \psi_N + \frac{f_0^2}{H_N}\left(\frac{\psi_{N-1} - \psi_N}{g'_{N-1/2}}\right) + \frac{f_0}{H_N}\eta_b, \tag{A2c}$$

where (A2b) holds for $k = 2, \ldots, N-1$, H_k is reference thickness of kth layer. The reduced gravity between each pair of adjacent layers is $g'_{k+1/2} = g(\rho_{k+1} - \rho_k)/\rho_0$, where ρ_0 is a reference density.

The baroclinic mode decomposition is defined by solutions of the following system of equations:

$$\frac{f_0^2}{H_1}\left(\frac{\hat{\psi}_2 - \hat{\psi}_1}{g'_{3/2}}\right) = \Gamma\hat{\psi}_1, \tag{A3a}$$

$$\frac{f_0^2}{H_k}\left(\frac{\hat{\psi}_{k-1} - \hat{\psi}_k}{g'_{k-1/2}} - \frac{\hat{\psi}_k - \hat{\psi}_{k+1}}{g'_{k+1/2}}\right) = \Gamma\hat{\psi}_k, \tag{A3b}$$

$$\frac{f_0^2}{H_N}\left(\frac{\hat{\psi}_{N-1} - \hat{\psi}_N}{g'_{N-1/2}}\right) = \Gamma\hat{\psi}_N. \tag{A3c}$$

The solution of this system is a sequence of N eigenvalues Γ_m, $m = 1, \ldots, N$, and corresponding orthogonal eigenvectors e_{mk} for $m, k = 1, \ldots, N$. The eigenvectors are a basis for the vertical structure of the QG streamfunction, i.e., for ψ_k, $k = 1, \ldots, N$. Formally, this may be expressed as

$$q_k = \sum_m \hat{q}_m e_{mk}, \tag{A4}$$

where $\hat{q}_m$, $m = 1, \ldots, N$ are the modal amplitudes and we normalize the eigenvectors so that their inner product satisfies

$$\sum_k H_k e_{mk} e_{nk} = \delta_{mn}. \tag{A5}$$

To decompose the nonlinear terms in the enstrophy budget, we must also evaluate the vertical integral of triads of baroclinic modes. These integrals are proportional to the mode interaction coefficient ε_{mln} defined in (16).

We will now decompose the enstrophy into mean and eddy components, and into baroclinic modes. First, note that the depth-integrated enstrophy is equal to the sum of the modal enstrophies, i.e.,

$$\sum_k \frac{1}{2} H_k q_k^2 = \sum_m \frac{1}{2}\hat{q}_m^2, \tag{A6}$$

which is the analog of Parseval's theorem in the vector space defined by the baroclinic modal eigenvectors. This implies that the enstrophy budget can be completely characterized by deriving evolution equations for the mean and eddy modal enstrophies.

We derive an evolution equation of the mean enstrophy by taking the mean of (A1),

$$\frac{\partial \overline{q}_k}{\partial t} + \nabla \cdot (\overline{\mathbf{u}}_k \overline{q}_k + \overline{\mathbf{u}'_k q'_k}) = \overline{\mathcal{D}}_k, \tag{A7}$$

and writing the mean PV as a sum of baroclinic modes following (A4),

$$\overline{q}_k = \sum_m \overline{\hat{q}}_m e_{mk}. \tag{A8}$$

To obtain an evolution equation for the enstrophy in a single mode n, we multiply (A7) by $\overline{\hat{q}}_n e_{nk} H_k$ and sum over k, using (A5) and (16),

$$\frac{\partial}{\partial t}\left(\frac{1}{2}\overline{\hat{q}}_n^2\right) + \sum_m \sum_l [\nabla \cdot (\overline{\hat{\mathbf{u}}}_m \overline{\hat{q}}_l) + \nabla \cdot (\overline{\hat{\mathbf{u}}'_m \hat{q}'_l})]\,\overline{\hat{q}}_n \varepsilon_{mln} = \overline{\hat{\mathcal{D}}}_n \overline{\hat{q}}_n. \tag{A9}$$

Next, we form an equation for the eddy PV by subtracting (A7) from (A1),

$$\frac{\partial q'_k}{\partial t} + \nabla \cdot (\overline{\mathbf{u}}_k q'_k + \mathbf{u}'_k \overline{q}'_k + \mathbf{u}'_k q'_k - \overline{\mathbf{u}'_k q'_k}) = \mathcal{D}'_k. \tag{A10}$$

We then follow a similar derivation as we did to obtain (A9), multiplying (A10) by $\hat{q}'_n e_{nk} H_k$ and summing over k, using (A5) and (16),

$$\frac{\partial}{\partial t}\left(\frac{1}{2}\overline{\hat{q}'^2_n}\right) + \sum_m \sum_l [\nabla \cdot \overline{(\overline{\hat{\mathbf{u}}}_m \hat{q}'_l)\hat{q}'_n} + \nabla \cdot \overline{(\hat{\mathbf{u}}'_m \overline{\hat{q}}_l)\hat{q}'_n} + \nabla \cdot \overline{(\hat{\mathbf{u}}'_m \hat{q}'_l)\hat{q}'_n}]\varepsilon_{mln} = \overline{\hat{\mathcal{D}}'_n \hat{q}'_n}. \tag{A11}$$

We now decompose the advective terms in (A9) and (A11) into enstrophy fluxes and enstrophy conversions. After some manipulation, we arrive at

$$\partial_t\left(\frac{1}{2}\overline{\hat{q}}_n^2\right) + \nabla \cdot \left[\sum_m \sum_l \ldots\right] = \overline{\hat{\mathcal{D}}}_n \overline{\hat{q}}_n + \underbrace{\sum_m \sum_l [\overline{\hat{\mathbf{u}}'_m \hat{q}'_l} \cdot \nabla \overline{\hat{q}}_n]\varepsilon_{mln}}_{\text{mean-to-eddy enstrophy conversion}} + \underbrace{\sum_m \sum_l [\overline{\hat{\mathbf{u}}}_m \overline{\hat{q}}_l \cdot \nabla \overline{\hat{q}}_n]\varepsilon_{mln}}_{\text{mode-to-mode mean enstrophy transfer}}, \quad \text{and} \tag{A12}$$

$$\partial_t\left(\frac{1}{2}\overline{\hat{q}'^2_n}\right) + \nabla \cdot \left[\sum_m \sum_l \ldots\right] = \overline{\hat{\mathcal{D}}'_n \hat{q}'_n} + \underbrace{\sum_m \sum_l [-\overline{\hat{\mathbf{u}}'_m \hat{q}'_l} \cdot \nabla \overline{\hat{q}}_n]\varepsilon_{mln}}_{\text{mean-to-eddy enstrophy conversion}} + \underbrace{\sum_m \sum_l [\overline{\hat{\mathbf{u}}'_m \hat{q}'_l \cdot \nabla \hat{q}'_n}]\varepsilon_{mln}}_{\text{mode-to-mode eddy enstrophy transfer}}. \tag{A13}$$

Finally, we specialize this enstrophy budget to our quasi-geostrophic model configuration, in which the time-mean flow and PV gradients are imposed and are horizontally uniform and constant in time

$$\overline{u}_k = U_k \hat{\mathbf{x}}, \qquad \overline{q}_k = \beta_k y, \tag{A14}$$

Thus, the mean enstrophy is fixed and (A9) is not directly relevant, while the eddy enstrophy budget simplifies to

$$\partial_t\left(\frac{1}{2}\overline{\hat{q}^2_n}\right) + \nabla \cdot \left[\sum_m \sum_l \ldots\right] = \overline{\hat{\mathcal{D}}_n \hat{q}_n} + \underbrace{\sum_m \sum_l [-\overline{\hat{v}_m \hat{q}_l}\hat{\beta}_n]\varepsilon_{mln}}_{\text{mean-to-eddy enstrophy conversion}} + \underbrace{\sum_m \sum_l [\overline{\hat{\mathbf{u}}_m \hat{q}_l \cdot \nabla \hat{q}_n}]\varepsilon_{mln}}_{\text{mode-to-mode eddy enstrophy transfer}}, \tag{A15}$$

for $m, l, n = 1, \ldots, N$. Here $\hat{\beta}_n$ denotes the nth baroclinic mode of the mean PV gradients, $\beta_k = \partial_y Q_k$.

REFERENCES

Arbic, B. K., R. B. Scott, G. R. Flierl, A. J. Morten, J. G. Richman, and J. F. Shriver, 2012: Nonlinear cascades of surface oceanic geostrophic kinetic energy in the frequency domain. *J. Phys. Oceanogr.*, **42**, 1577–1600, https://doi.org/10.1175/JPO-D-11-0151.1.

Armitage, T. W. K., G. E. Manucharyan, A. A. Petty, R. Kwok, and A. F. Thompson, 2020: Enhanced eddy activity in the Beaufort Gyre in response to sea ice loss. *Nat. Commun.*, **11**, 761, https://doi.org/10.1038/s41467-020-14449-z.

Blumsack, S. L., and P. J. Gierasch, 1972: Mars: The effects of topography on baroclinic instability. *J. Atmos. Sci.*, **29**, 1081–1089, https://doi.org/10.1175/1520-0469(1972)029<1081:MTEOTO>2.0.CO;2.

Brannigan, L., H. Johnson, C. Lique, J. Nycander, and J. Nilsson, 2017: Generation of subsurface anticyclones at Arctic surface fronts due to a surface stress. *J. Phys. Oceanogr.*, **47**, 2653–2671, https://doi.org/10.1175/JPO-D-17-0022.1.

Cassianides, A., C. Lique, and A. Korosov, 2021: Ocean eddy signature on SAR-derived sea ice drift and vorticity. *Geophys. Res. Lett.*, **48**, e2020GL092066, https://doi.org/10.1029/2020GL092066.

Cavalieri, D. J., and C. L. Parkinson, 2012: Arctic Sea ice variability and trends, 1979–2010. *Cryosphere*, **6**, 881–889, https://doi.org/10.5194/tc-6-881-2012.

Charney, J. G., 1947: The dynamics of long waves in a baroclinic westerly current. *J. Atmos. Sci.*, **4**, 136–162, https://doi.org/10.1175/1520-0469(1947)004<0136:TDOLWI>2.0.CO;2.

Cole, S. T., M.-L. Timmermans, J. M. Toole, R. A. Krishfield, and F. T. Thwaites, 2014: Ekman veering, internal waves, and turbulence observed under Arctic Sea ice. *J. Phys. Oceanogr.*, **44**, 1306–1328, https://doi.org/10.1175/JPO-D-12-0191.1.

D'Asaro, E. A., 1988: Observations of small eddies in the Beaufort Sea. *J. Geophys. Res.*, **93**, 6669–6684, https://doi.org/10.1029/JC093iC06p06669.

Dewey, S., J. Morison, R. Kwok, S. Dickinson, D. Morison, and R. Andersen, 2018: Arctic ice-ocean coupling and gyre equilibration observed with remote sensing. *Geophys. Res. Lett.*, **45**, 1499–1508, https://doi.org/10.1002/2017GL076229.

Doddridge, E. W., G. Meneghello, J. Marshall, J. Scott, and C. Lique, 2019: A three-way balance in the Beaufort Gyre: The ice-ocean governor, wind stress, and eddy diffusivity. *J. Geophys. Res. Oceans*, **124**, 3107–3124, https://doi.org/10.1029/2018JC014897.

Eady, E. T., 1949: Long waves and cyclone waves. *Tellus*, **1**, 33–52, https://doi.org/10.3402/tellusa.v1i3.8507.

Hart, J. E., and P. D. Killworth, 1976: On open ocean baroclinic instability in the Arctic. *Deep-Sea Res. Oceanogr. Abstr.*, **23**, 637–645, https://doi.org/10.1016/0011-7471(76)90006-1.

Holland, P. R., and R. Kwok, 2012: Wind-driven trends in Antarctic sea-ice drift. *Nat. Geosci.*, **5**, 872–875, https://doi.org/10.1038/ngeo1627.

Hunkins, K. L., 1974: Subsurface eddies in the Arctic Ocean. *Deep-Sea Res. Oceanogr. Abstr.*, **21**, 1017–1033, https://doi.org/10.1016/0011-7471(74)90064-3.

Isachsen, P. E., 2011: Baroclinic instability and eddy tracer transport across sloping bottom topography: How well does a modified Eady model do in primitive equation simulations? *Ocean Modell.*, **39**, 183–199, https://doi.org/10.1016/j.ocemod.2010.09.007.

Johnson, G. C., S. Schmidtko, and J. M. Lyman, 2012: Relative contributions of temperature and salinity to seasonal mixed layer density changes and horizontal density gradients. *J. Geophys. Res.*, **117**, C04015, https://doi.org/10.1029/2011JC007651.

Kenigson, J. S., R. Gelderloos, and G. E. Manucharyan, 2021: Vertical structure of the Beaufort Gyre halocline and the crucial role of the depth-dependent eddy diffusivity. *J. Phys. Oceanogr.*, **51**, 845–860, https://doi.org/10.1175/JPO-D-20-0077.1.

Kozlov, I. E., A. V. Artamonova, G. E. Manucharyan, and A. A. Kubryakov, 2019: Eddies in the western Arctic Ocean from spaceborne SAR observations over open ocean and marginal ice zones. *J. Geophys. Res. Oceans*, **124**, 6601–6616, https://doi.org/10.1029/2019JC015113.

Kubryakov, A. A., I. E. Kozlov, and G. E. Manucharyan, 2021: Large mesoscale eddies in the western Arctic Ocean from satellite altimetry measurements. *J. Geophys. Res. Oceans*, **126**, e2020JC016670, https://doi.org/10.1029/2020JC016670.

Liang, X., M. Spall, and C. Wunsch, 2017: Global ocean vertical velocity from a dynamically consistent ocean state estimate. *J. Geophys. Res. Oceans*, **122**, 8208–8224, https://doi.org/10.1002/2017JC012985.

Manley, T. O., and K. Hunkins, 1985: Mesoscale eddies of the Arctic Ocean. *J. Geophys. Res.*, **90**, 4911–4930, https://doi.org/10.1029/JC090iC03p04911.

Manucharyan, G. E., and M.-L. Timmermans, 2013: Generation and separation of mesoscale eddies from surface ocean fronts. *J. Phys. Oceanogr.*, **43**, 2545–2562, https://doi.org/10.1175/JPO-D-13-094.1.

——, and M. A. Spall, 2016: Wind-driven freshwater buildup and release in the Beaufort Gyre constrained by mesoscale eddies. *Geophys. Res. Lett.*, **43**, 273–282, https://doi.org/10.1002/2015GL065957.

——, and P. E. Isachsen, 2019: Critical role of continental slopes in halocline and eddy dynamics of the Ekman-driven Beaufort Gyre. *J. Geophys. Res. Oceans*, **124**, 2679–2696, https://doi.org/10.1029/2018JC014624.

——, and A. F. Thompson, 2022: Heavy footprints of upper-ocean eddies on weakened Arctic sea ice in marginal ice zones. *Nat. Commun.*, **13**, 2147, https://doi.org/10.1038/s41467-022-29663-0.

——, M. A. Spall, and A. F. Thompson, 2016: A theory of the wind-driven Beaufort Gyre variability. *J. Phys. Oceanogr.*, **46**, 3263–3278, https://doi.org/10.1175/JPO-D-16-0091.1.

——, A. F. Thompson, and M. A. Spall, 2017: Eddy memory mode of multidecadal variability in residual-mean ocean circulations with application to the Beaufort Gyre. *J. Phys. Oceanogr.*, **47**, 855–866, https://doi.org/10.1175/JPO-D-16-0194.1.

——, R. Lopez-Acosta, and M. M. Wilhelmus, 2022: Spinning ice floes reveal intensification of mesoscale eddies in the western Arctic Ocean. *Sci. Rep.*, **12**, 7070, https://doi.org/10.1038/s41598-022-10712-z.

McCalpin, J. D., 1987: On the adjustment of azimuthally perturbed vortices. *J. Geophys. Res.*, **92**, 8213–8225, https://doi.org/10.1029/JC092iC08p08213.

McPhee, M. G., 2012: Advances in understanding ice–ocean stress during and since AIDJEX. *Cold Reg. Sci. Technol.*, **76–77**, 24–36, https://doi.org/10.1016/j.coldregions.2011.05.001.

McWilliams, J. C., 1990: The vortices of geostrophic turbulence. *J. Fluid Mech.*, **219**, 387–404, https://doi.org/10.1017/S0022112090002993.

——, 2016: Submesoscale currents in the ocean. *Proc. Roy. Soc.*, **A472**, 20160117, http://doi.org/10.1098/rspa.2016.0117.

Meneghello, G., J. Marshall, S. T. Cole, and M.-L. Timmermans, 2017: Observational inferences of lateral eddy diffusivity in the halocline of the Beaufort Gyre. *Geophys. Res. Lett.*, **44**, 12 331–12 338, https://doi.org/10.1002/2017GL075126.

——, ——, J.-M. Campin, E. Doddridge, and M.-L. Timmermans, 2018a: The ice-ocean governor: Ice-ocean stress feedback limits Beaufort Gyre spin-up. *Geophys. Res. Lett.*, **45**, 11 293–11 299, https://doi.org/10.1029/2018GL080171.

——, ——, M.-L. Timmermans, and J. Scott, 2018b: Observations of seasonal upwelling and downwelling in the Beaufort Sea mediated by sea ice. *J. Phys. Oceanogr.*, **48**, 795–805, https://doi.org/10.1175/JPO-D-17-0188.1.

——, E. Doddridge, J. Marshall, J. Scott, and J.-M. Campin, 2020: Exploring the role of the "ice–ocean governor" and mesoscale eddies in the equilibration of the Beaufort Gyre: Lessons from observations. *J. Phys. Oceanogr.*, **50**, 269–277, https://doi.org/10.1175/JPO-D-18-0223.1.

——, J. Marshall, C. Lique, P. E. Isachsen, E. Doddridge, J.-M. Campin, H. Regan, and C. Talandier, 2021: Genesis and decay of mesoscale baroclinic eddies in the seasonally ice-covered interior Arctic Ocean. *J. Phys. Oceanogr.*, **51**, 115–129, https://doi.org/10.1175/JPO-D-20-0054.1.

Nurser, A. J. G., and S. Bacon, 2014: The Rossby radius in the Arctic Ocean. *Ocean Sci.*, **10**, 967–975, https://doi.org/10.5194/os-10-967-2014.

Ou, H. W., and A. L. Gordon, 1986: Spin-down of baroclinic eddies under sea ice. *J. Geophys. Res.*, **91**, 7623–7630, https://doi.org/10.1029/JC091iC06p07623.

Pavía, E. G., and M. López, 1994: Long-term evolution of elongated warm eddies. *J. Phys. Oceanogr.*, **24**, 2201–2208, https://doi.org/10.1175/1520-0485(1994)024<2201:LTEOEW>2.0.CO;2.

Proshutinsky, A., and Coauthors, 2009: Beaufort Gyre freshwater reservoir: State and variability from observations. *J. Geophys. Res.*, **114**, C00A10, https://doi.org/10.1029/2008JC005104.

——, and Coauthors, 2019: Analysis of the Beaufort Gyre freshwater content in 2003–2018. *J. Geophys. Res. Oceans*, **124**, 9658–9689, https://doi.org/10.1029/2019JC015281.

——, R. Krishfield, and M.-L. Timmermans, 2020: Introduction to special collection on Arctic Ocean modeling and observational synthesis (FAMOS) 2: Beaufort gyre phenomenon. *J. Geophys. Res. Oceans*, **125**, e2019JC015400, https://doi.org/10.1029/2019JC015400.

Regan, H. C., C. Lique, and T. W. Armitage, 2019: The Beaufort Gyre extent, shape, and location between 2003 and 2014 from satellite observations. *J. Geophys. Res. Oceans*, **124**, 844–862, https://doi.org/10.1029/2018JC014379.

——, ——, C. Talandier, and G. Meneghello, 2020: Response of total and eddy kinetic energy to the recent spinup of the Beaufort Gyre. *J. Phys. Oceanogr.*, **50**, 575–594, https://doi.org/10.1175/JPO-D-19-0234.1.

Serreze, M. C., and J. Stroeve, 2015: Arctic Sea ice trends, variability and implications for seasonal ice forecasting. *Philos. Trans. Roy. Soc.*, **A373**, 20140159, https://doi.org/10.1098/rsta.2014.0159.

Shrestha, K., and G. E. Manucharyan, 2022: Parameterization of submesoscale mixed layer restratification under sea ice. *J. Phys. Oceanogr.*, **52**, 419–435, https://doi.org/10.1175/JPO-D-21-0024.1.

Smith, D. C., IV, J. W. Lavelle, and H. J. S. Fernando, 2002: Arctic Ocean mixed-layer eddy generation under leads in sea ice. *J. Geophys. Res.*, **107**, 3103, https://doi.org/10.1029/2001JC000822.

Smith, K. S., 2007: The geography of linear baroclinic instability in Earth's oceans. *J. Mar. Res.*, **65**, 655–683, https://doi.org/10.1357/002224007783649484.

——, and G. K. Vallis, 2001: The scales and equilibration of midocean eddies: Freely evolving flow. *J. Phys. Oceanogr.*, **31**, 554–571, https://doi.org/10.1175/1520-0485(2001)031<0554:TSAEOM>2.0.CO;2.

Spall, M. A., 2020: Potential vorticity dynamics of the Arctic halocline. *J. Phys. Oceanogr.*, **50**, 2491–2506, https://doi.org/10.1175/JPO-D-20-0056.1.

——, R. S. Pickart, P. S. Fratantoni, and A. J. Plueddemann, 2008: Western Arctic shelfbreak eddies: Formation and transport. *J. Phys. Oceanogr.*, **38**, 1644–1668, https://doi.org/10.1175/2007JPO3829.1.

Spreen, G., R. Kwok, and D. Menemenlis, 2011: Trends in Arctic Sea ice drift and role of wind forcing: 1992–2009. *Geophys. Res. Lett.*, **38**, L19501, https://doi.org/10.1029/2011GL048970.

Thomas, L. N., A. Tandon, and A. Mahadevan, 2008: Submesoscale processes and dynamics. *Ocean Modeling in an Eddying Regime*, *Geophys. Monogr.*, Vol. 177, Amer. Geophys. Union, 17–38, https://doi.org/10.1029/177GM04.

Vallis, G. K., 2017: *Atmospheric and Oceanic Fluid Dynamics*. 2nd ed. Cambridge University Press, 946 pp.

Wang, Q., J. Marshall, J. Scott, G. Meneghello, S. Danilov, and T. Jung, 2019: On the feedback of ice–ocean stress coupling from geostrophic currents in an anticyclonic wind regime over the Beaufort Gyre. *J. Phys. Oceanogr.*, **49**, 369–383, https://doi.org/10.1175/JPO-D-18-0185.1.

——, N. V. Koldunov, S. Danilov, D. Sidorenko, C. Wekerle, P. Scholz, I. L. Bashmachnikov, and T. Jung, 2020: Vertical scales and dynamics of eddies in the Arctic Ocean's Canada basin. *Geophys. Res. Lett.*, **47**, e2020GL088550, https://doi.org/10.1029/2020GL088550.

Zhao, M., and M.-L. Timmermans, 2015: Vertical scales and dynamics of eddies in the Arctic Ocean's Canada basin. *J. Geophys. Res. Oceans*, **120**, 8195–8209, https://doi.org/10.1002/2015JC011251.

——, ——, S. Cole, R. Krishfield, A. Proshutinsky, and J. Toole, 2014: Characterizing the eddy field in the Arctic Ocean halocline. *J. Geophys. Res. Oceans*, **119**, 8800–8817, https://doi.org/10.1002/2014JC010488.

——, ——, ——, ——, and J. Toole, 2016: Evolution of the eddy field in the Arctic Ocean's Canada basin, 2005–2015. *Geophys. Res. Lett.*, **43**, 8106–8114, https://doi.org/10.1002/2016GL069671.

——, ——, R. Krishfield, and G. Manucharyan, 2018: Partitioning of kinetic energy in the Arctic Ocean's Beaufort Gyre. *J. Geophys. Res. Oceans*, **123**, 4806–4819, https://doi.org/10.1029/2018JC014037.

Zhong, W., M. Steele, J. Zhang, and J. Zhao, 2018: Greater role of geostrophic currents in Ekman dynamics in the western Arctic Ocean as a mechanism for Beaufort Gyre stabilization. *J. Geophys. Res. Oceans*, **123**, 149–165, https://doi.org/10.1002/2017JC013282.